

RESEARCH ARTICLE

Neural tube closure requires the endocytic receptor Lrp2 and its functional interaction with intracellular scaffolds

Izabela Kowalczyk¹, Chanjae Lee², Elisabeth Schuster³, Josefine Hoeren³, Valentina Trivigno³, Levin Riedel¹, Jessica Görne¹, John B. Wallingford², Annette Hammes^{1,*} and Kerstin Feistel^{3,*}‡

ABSTRACT

Pathogenic mutations in the endocytic receptor LRP2 in humans are associated with severe neural tube closure defects (NTDs) such as anencephaly and spina bifida. Here, we have combined analysis of neural tube closure in mouse and in the African Clawed Frog *Xenopus laevis* to elucidate the etiology of Lrp2-related NTDs. *Lrp2* loss of function impaired neuroepithelial morphogenesis, culminating in NTDs that impeded anterior neural plate folding and neural tube closure in both model organisms. Loss of Lrp2 severely affected apical constriction as well as proper localization of the core planar cell polarity (PCP) protein Vangl2, demonstrating a highly conserved role of the receptor in these processes, which are essential for neural tube formation. In addition, we identified a novel functional interaction of Lrp2 with the intracellular adaptor proteins Shroom3 and Gipc1 in the developing forebrain. Our data suggest that, during neurulation, motifs within the intracellular domain of Lrp2 function as a hub that orchestrates endocytic membrane removal for efficient apical constriction, as well as PCP component trafficking in a temporospatial manner.

KEY WORDS: Lrp2, Gipc1, Vangl2, Neural tube closure, Mouse, *Xenopus*

INTRODUCTION

The vertebrate forebrain originates from a simple sheet of neuroepithelial cells and subsequently forms the largest part of the brain. The anterior neural plate (NP) evaginates, bends and then progressively fuses along the dorsal midline to establish the neural tube (Nikolopoulou et al., 2017). Defects in these processes during early brain development lead to a range of congenital brain malformations in humans, including holoprosencephaly (HPE) and anencephaly. Several environmental and genetic risk factors have been identified as possible causes of structural brain anomalies (Greene and Copp, 2014; Wallingford et al., 2013).

Low-density lipoprotein (LDL) receptor-related protein 2 (LRP2, also known as megalin; Saito et al., 1994) is associated with severe forebrain defects. LRP2 is a multifunctional cell surface receptor and localizes to the apical surface of epithelia (Nykjaer and

Willnow, 2002). All LRP2 orthologs share a large extracellular and a shorter intracellular domain with typical NPxY endocytosis motifs (Chen et al., 1990), but also phosphorylation and PDZ-binding motifs relevant for interactions with intracellular adaptors and scaffolding proteins (Gotthardt et al., 2000; Naccache et al., 2006). Humans with autosomal recessive *LRP2* gene defects develop Donnai-Barrow syndrome (DBS) presenting with craniofacial anomalies (ocular hypertelorism and enlarged fontanelle) and forebrain defects, such as agenesis of the corpus callosum (Kantarci et al., 2007; Ozdemir et al., 2020) and microforms of HPE (Rosenfeld et al., 2010). Most abnormalities in individuals with *LRP2* gene mutations are also present in the LRP2-deficient mouse (Cases et al., 2015; Hammes et al., 2005; Kur et al., 2014; Spoelgen et al., 2005; Wicher and Aldskogius, 2008), making it a valuable model for studying the mechanistic basis of this disorder.

In addition to HPE caused by impaired SHH signaling in the ventral forebrain (Christ et al., 2012), LRP2-deficient mice display defects of the anterior dorsolateral neural tube as well as spinal cord anomalies that cannot be explained by loss of SHH signaling (Kur et al., 2014; Wicher and Aldskogius, 2008; Ybot-Gonzalez et al., 2002). We and other labs have demonstrated that LRP2-deficient mice present with a dilated dorsal neural tube and cranial neural tube closure defects (NTDs; Kur et al., 2014; Sabatino et al., 2017). Human *LRP2* variants have also been identified in individuals with NTDs, ultimately leading to anencephaly and myelomeningocele (open spina bifida; Rebekah Prasoon et al., 2018; Renard et al., 2019).

Neural tube closure (NTC) and morphogenesis is marked by extensive and rapid cell and tissue rearrangements, driven by morphogenetic events such as cell migration, intercalation and cell shape changes (Wallingford, 2005). We used the African Clawed Frog *Xenopus laevis* to study morphogenetic events during neurulation, a process that closely resembles that of humans and mice, but can be manipulated and observed in the Petri dish *in vivo*.

As LRP2 is a candidate gene for NTDs, we asked whether Lrp2-mediated endocytosis was required for dynamic cell behaviors during NTC. We show here for the first time that there are common NTDs in Lrp2-deficient *Xenopus* and mouse embryos. Loss of LRP2-mediated endocytosis impaired apical constriction and caused aberrant localization of the core planar cell polarity (PCP) component Vangl2 in both model organisms. Lrp2 functionally interacted with intracellular adaptor and scaffold proteins to exert its function in NTC.

RESULTS

Constricting forebrain neuroepithelial cells show enriched localization of LRP2 on the apical surface


First, *lrp2* expression was analyzed at relevant stages of *Xenopus* development. Lrp2 protein is maternally expressed and protein levels increase with the onset of zygotic *lrp2* transcription

¹Disorders of the Nervous System, Max Delbrück Center for Molecular Medicine in the Helmholtz Association, Robert Rössle Strasse 10, 13125 Berlin, Germany.

²Department of Molecular Biosciences, The University of Texas at Austin, Austin, TX 78712, USA. ³University of Hohenheim, Institute of Biology, Department of Zoology, Garbenstrasse 30, 70599 Stuttgart, Germany.

*Both senior authors have contributed equally to this work

‡Authors for correspondence (k.feistel@uni-hohenheim.de, hammes@mdc-berlin.de)

 I.K., 0000-0002-1476-7531; A.H., 0000-0003-1663-8378; K.F., 0000-0003-3397-8972

(Fig. S1A; Peshkin et al., 2019 preprint; Session et al., 2016). *lrp2* was also expressed in DBS-relevant organ anlagen such as the brain, eye, otic vesicle and pronephros (Fig. S1B).

Neuroepithelial cells undergo shape changes to apically constrict and form hinge points that ultimately allow proper tissue morphogenesis during neural tube upfolding. *lrp2* transcripts were detected in the NP (Fig. 1A) and the protein localized in *Xenopus* (Fig. 1B) and mouse (Fig. 1C) neuroepithelial cells during early forebrain development. The most prominent signals for Lrp2 were detected in apically constricting cells, which in *Xenopus* are first apparent along the borders of the NP (arrowheads in Fig. 1B,B') and appear upon formation of the optic evagination (OE) in the mouse (Fig. 1C'). Stimulated emission depletion (STED) microscopy revealed LRP2 localization concentrated in the periciliary region (Fig. 1D), a highly endocytic plasma membrane domain at the base of the primary cilium (Benmerah, 2013; Molla-Herman et al., 2010). The highly specific localization of Lrp2/LRP2 in neuroepithelial cells, correlating with cell shape changes during apical constriction (AC), suggested a role for this receptor in cellular remodeling to enable tissue morphogenesis.

Loss of *Lrp2* disrupts neural tube morphogenesis

We next examined neurulation in *Xenopus* upon *lrp2* loss of function and in mouse null mutants for *Lrp2*. Neural tube morphology of *Lrp2*^{-/-} mouse embryos was altered at embryonic day (E) 8.5 compared with wild-type controls, as observed using

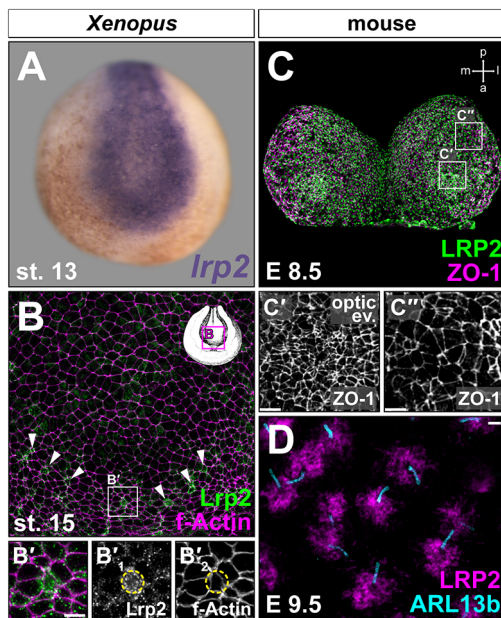


Fig. 1. *Lrp2* is expressed in the neuroepithelium and increased in constricting cells. (A–D) *lrp2* mRNA (A) and protein (B–D) expression analyzed by *in situ* hybridization and immunofluorescence, respectively. Neurula stage (st.) embryos (frontal views, dorsal upwards). (A) Neural *lrp2* expression. (B) Stage 15 forebrain region; Lrp2 is expressed in most cells (outlined by F-actin); single cells with high Lrp2 levels are located along the anterior rim of neural folds (NFs; arrowheads). (B') Magnification of boxed region in B; increased Lrp2 levels are found in cells with small apical surface (circled in single channels B'1 and B'2). (C) LRP2 is detected throughout E8.5 anterior NFs, concentrated in areas undergoing apical constriction. Compare C' (constricted cells in optic evagination) with C'' (dorsolateral cells with larger cell surface). ZO-1 marks cell boundaries. (D) STED imaging; LRP2 is condensed around neuroepithelial primary cilia (ARL13b⁺) at E9.5. Scale bars: 10 μm in B', C', C''; 1 μm in D.

scanning electron microscopy (Fig. 2A–F). Following neural tube morphogenesis in wild-type and somite-matched mutant embryos from 6- to 8-somite stages, we detected a delay and ultimately a deficit in OE formation in the developing forebrain of *Lrp2*^{-/-} mice (Fig. 2D–F). At the 8-somite stage, mutant neural folds were less elevated (Fig. 2F) compared with controls (Fig. 2C). In wild-type embryos at E9.5, the anterior neural tube is closed and midline separation of the forebrain vesicles starts. Compared with the wild type (Fig. S2A), *Lrp2* null mutants at this stage had either severely dilated or open neural tubes. At E18.5, when a proper skin-covered skull had formed in wild-type embryos, *Lrp2* null mutants had either a small skull and a dilated fontanelle through which dorsal midline (dML) tissue, such as choroid plexus, protruded, or an atypical form of anencephaly (Fig. S2A; compare with Willnow et al., 1996). Evaluation of mutants between E9.5 and E18.5 suggested that embryos with dilated neural tubes at E9.5 could follow two developmental paths: (1) they could develop an increasingly dilated dML, culminating in defective dML-derived organs and impaired fontanelle closure; or (2) they could also show impaired anterior neuropore (ANP) closure, leading to further opening of the ANP, eventually exposing anterior neural tissue and culminating in tissue atrophy and atypical anencephaly. Few embryos with open neural tubes at E9.5 might catch up and continue down path (2); however, numbers suggested that they die at mid-gestation due to cardiovascular defects (Baardman et al., 2016; Christ et al., 2020), as resorption of embryos was frequently observed.

Integrity of the neuroepithelium was further evaluated in coronal sections of anterior neural tissue at E8.5. Neural folds of 10-somite wild-type embryos were elevated and staining for acetylated α -tubulin showed the distribution of stabilized tubulin, highlighting the apicobasal axis of the pseudostratified neuroepithelial sheet (Fig. 2G,G₁). In somite-matched *Lrp2* null mutants, neural fold elevation was impaired and the appearance of the neuroepithelium (Fig. 2H,H₁) suggested impaired apicobasal elongation, a common feature in cells with defective AC.

In *Xenopus laevis*, a translation-blocking morpholino oligomer (MO), binding within the 5' UTR of *lrp2.L*, was targeted to neural tissue by injecting into the animal pole of dorsal blastomeres of 4- to 8-cell embryos. Unilateral injections were performed such that the uninjected contralateral sides served as an internal control. This led to a reliable loss of Lrp2 protein in targeted cells, comparable with *Lrp2*^{-/-} mice (Fig. S1C,D,E) and impaired NP folding in all embryos in which lineage tracer fluorescence confirmed correct targeting of NP cells (Movie 1). While pigment accumulation along the border of neural/non-neural tissue illustrated the formation of hinge points on the uninjected side, hinge point formation was missing contralaterally (green versus red dashed line in Fig. 2I). When the neural folds contacted each other in controls, rostral and caudal neural folds of bilaterally injected embryos stayed apart (Fig. 2J). Despite considerable caudal neural fold convergence, transverse sections revealed that the floor plate, which was narrow with apically constricted cells in controls (Fig. 2J',J'₁), featured cells with large apical surfaces and remained wide, preventing close apposition of the neural folds (Fig. 2J'',J''₁). These results confirmed that loss of LRP2/Lrp2 in mouse and *Xenopus* led to NTDs.

To quantify the neural phenotype caused by *Lrp2* deficiency in *Xenopus*, the NP was labeled using the pan-neural marker *sox3*; NP width in the forebrain region was measured on either side of the midline and ratios between control and injected side were plotted. (Fig. 2K–N). Whereas uninjected control NPs had a ratio around 1 (Fig. 2K,N), *lrp2* loss of function significantly impaired NP

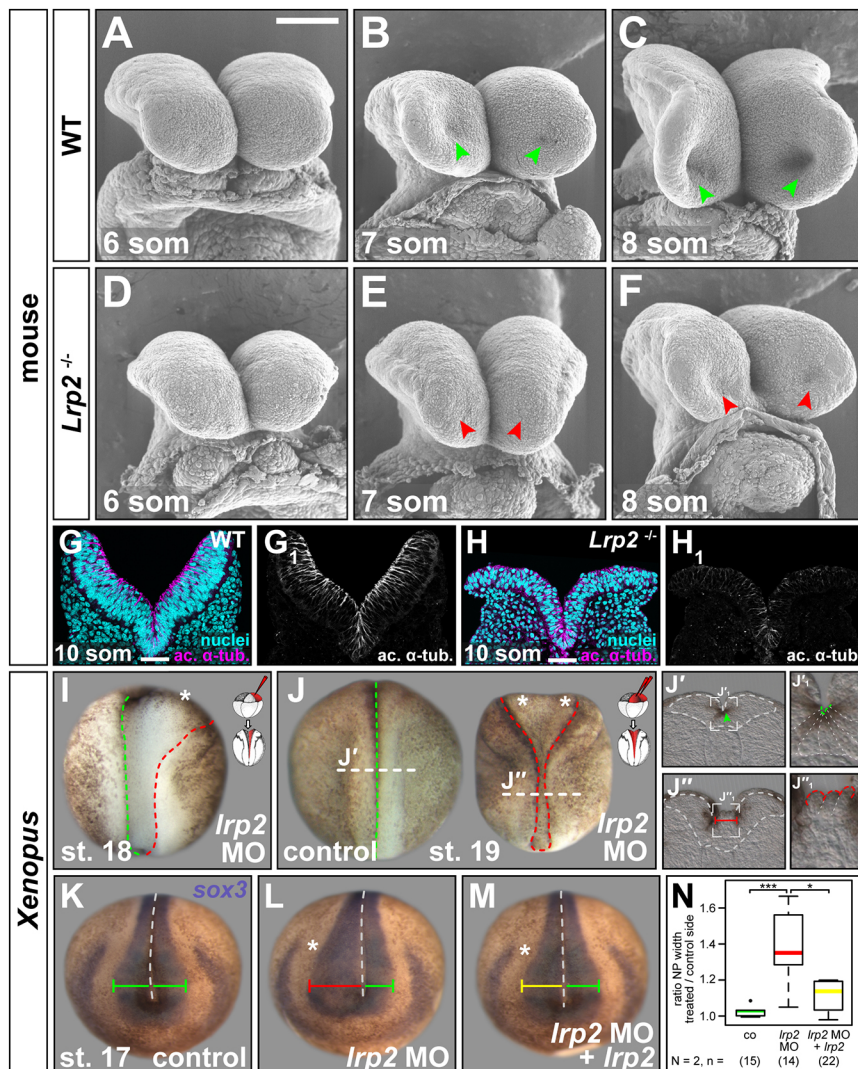


Fig. 2. *Lrp2* is required for proper neuroepithelial morphogenesis and neural tube closure. Neural plate (NP) morphology. (A-F) Scanning electron micrographs of neural folds (NFs) from E8.5 wild-type (WT) and *Lrp2*^{-/-} mouse embryos at the 6-, 7- and 8-somite (som) stages (st.), frontal views. (A-C) Wild-type NFs are progressively elevated and optic evagination is initiated (arrowheads in B,C). (D-F) Narrower NFs have delayed elevation and there is impaired optic evagination in mutants (arrowheads in E,F). (G,H) Immunofluorescence staining detecting acetylated α -tubulin (ac. α -tub.) and DAPI-stained nuclei on coronal sections of 10-somite wild-type and *Lrp2*^{-/-} mouse NFs. Scale bars: 100 μ m in A-F; 50 μ m in G,H. (I,J) Dotted lines indicate normal (green) and abnormal (red) positioning of the border between neural and non-neural ectoderm. (I) Morpholino oligomer targeting *lrp2.L* (*lrp2* MO) injected as indicated. Impaired hinge point formation and NF convergence on the injected side are indicated (asterisk). (J) Closely apposed NFs in control at stage 19. Open anterior and posterior NFs, and a short anteroposterior axis are formed upon bilateral injection (asterisks); embryos were photographed at the same magnification. (J',J'',J''',J''') Transverse sections and magnifications thereof; levels are as indicated in J. Green markers indicate normal floor plate width (J') and apical cell surfaces (J'''); red markers indicate wide floor plate (J'') and abnormally wide apical cell surfaces (J'''). (K-M) *In situ* hybridization for *sox3*; normal NP width (green bar) is found in control (K); *lrp2* MO-impaired NP narrowing (red bar, L) was partially rescued (yellow bar) by re-introduction of *lrp2* (M). (N) Graphical representation of results from K-M (box plot, Wilcoxon rank sum test).

narrowing (Fig. 2L,N). Owing to its size of 4663 amino acids, expressing a full-length construct of *Xenopus lrp2* was not feasible; therefore, we used a well-characterized extracellularly truncated construct of human *LRP2*, containing the fourth ligand-binding domain as well as transmembrane and intracellular domains (Yuseff et al., 2007), which we refer to as *lrp2* in rescue experiments. Reintroducing *lrp2* on the injected side partially rescued this NP defect (Fig. 2M,N), confirming specificity of the MO approach and supporting a direct function of *Lrp2* in neural tube morphogenesis.

Specificity of the *lrp2* MO was further affirmed by CRISPR/Cas9-mediated genome editing of *lrp2.L* (Fig. S2B), as injection of Cas9 ribonucleic particles (CRNPs) assembled with two different single guide (sg) RNAs into zygotes recapitulated the shortened and widened NP of morphants (Fig. S2C-F), a phenotype that was rescued by co-injection of *lrp2* (compare with Fig. 7L). *Lrp2* protein reduction (Fig. S2G-J), as well as sequencing of targeted regions (Fig. S2K,L), confirmed successful *lrp2* loss of function upon CRISPR/Cas9 treatment.

***Lrp2* is cell-autonomously required for efficient apical constriction**

Hinge point formation leading to NP bending and thus neural fold apposition is driven by AC, i.e. narrowing of the apical surface and widening of basolateral cell aspects (Martin and Goldstein, 2014).

Impaired neural fold apposition and loss of hinge points in *Xenopus* prompted us to examine whether *Lrp2* plays a role in regulating such cell shape changes. We analyzed the morphology of *Xenopus* neuroepithelial cells upon injection of *lrp2* MO (Fig. 3A-F). F-actin staining revealed a much larger apical surface in cells that had received *lrp2* MO compared with uninjected contralateral cells (Fig. 3A,A₁). This was especially striking in the region of the OE where uninjected cells were maximally constricted, while the surface of adjacent morphant cells was larger. This phenotype was quantified by measuring the apical cell surface and calculating ratios between the mean size of uninjected and injected cells within the same area of individual embryos (Fig. 3B-E,B₁-D₁). Whereas injection of lineage tracer alone had no effect on cell surface area (Fig. 3B,E), injection of *lrp2* MO resulted in cell surfaces around three times the size of uninjected constricting cells (Fig. 3C,E). Reintroduction of *lrp2* significantly ameliorated defective constriction of *lrp2* morphant cells (Fig. 3D,E). The clear difference in size between cells on the injected and uninjected sides, as well as in clonally distributed targeted cells (Fig. 3F), strongly indicated that *Lrp2* depletion in *Xenopus* cell-autonomously impaired AC.

Consistent with these findings in *Xenopus*, significantly larger cell surfaces were detected in *LRP2*-deficient mouse forebrain neuroepithelial cells compared with wild type (Fig. 3G-I). The differences in apical surface size were obvious within the

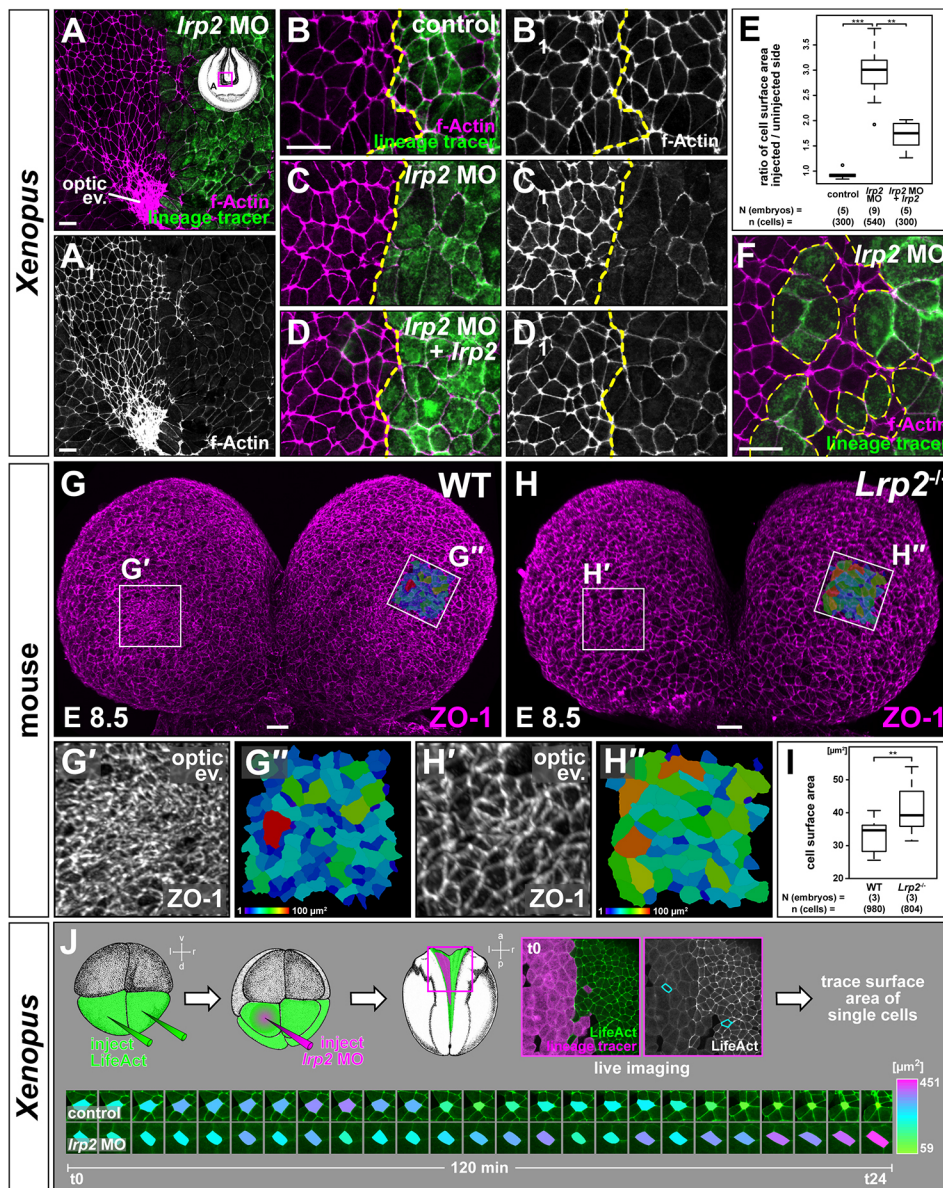


Fig. 3. *Lrp2* is cell-autonomously required for efficient apical constriction. Apical constriction (AC) in forebrain neural plate (NP) cells. (A,A') F-actin revealed a larger apical cell surface in *Irp2* morpholino oligomer (MO)-injected cells (identified by lineage tracer fluorescence) compared with the uninjected side; there was a lack of AC in the optic evagination (ev.) area on the injected side. (B-E) Quantification of cell surface areas in unilaterally injected lineage tracer-only controls (B,B'), *Irp2* morphants (C,C') and morphants with re-introduced *Irp2* (D,D'). (E) Cell surface area ratios calculated between injected and uninjected sides; box plot and Wilcoxon rank sum test. (F) The intermingling of constricting NP cells with *Irp2* morphant cells demonstrates cell autonomy of AC failure. (G,H) Frontal views of the forebrain area of wild-type (WT; G) and *Lrp2*^{-/-} (H) 7-somite stage mouse embryos at E8.5; ZO-1 delineates cell borders. (G',H') Magnification of optic evagination area, indicated in G,H; cell surface area was increased in mutants. (G'',H'') Color-coded maps (areas indicated in G,H) visualize cell surface area. (I) Graphical representation of results from G'',H''; four areas from each embryo were analyzed; box plot and Student's *t*-test. (J) Live imaging (Movie 2) using LifeAct indicates a failure of AC in morphant cells, despite actin dynamics. Cell surface area measurements revealed size fluctuations; final AC occurred in control cells only. Scale bars: 25 μ m in A-D,F; 20 μ m in G,H.

OE. Although cells were highly constricted in the wild type (Fig. 3G,G',G'',I), mutant cells in the same area had significantly larger cell surfaces (Fig. 3H-I), suggesting that LRP2 deficiency also impairs AC in the mouse.

To analyze the effect of *Lrp2* deficiency on the dynamic cell shape changes during AC, we applied live imaging on *Xenopus* embryos injected bilaterally with LifeAct, an *in vivo* marker for actin dynamics, combined with unilateral *Irp2* MO injection (Fig. 3J; Movie 2). Measurement of cell surface areas over time demonstrated size fluctuation in control cells that finalized AC (Fig. 3J; Fig. S3). Morphant cell size also fluctuated, but cells failed to constrict apically. However, actin dynamics, as judged by transient protrusions and actin movement within cells, were not affected (Movie 2). The data indicate that *Lrp2* does not mediate AC by controlling actin dynamics.

Remodeling of apical membrane is impaired in *Lrp2*-deficient cells

AC decreases apical surface area, thus creating a surplus of apical membrane that arranges into structures such as ruffles, filamentous

spikes/villi or spherical blebs. These serve as locations for short-term storage of membrane prior to its endocytic uptake (Gauthier et al., 2012). Microvillous membrane protrusions have been observed on apically constricting cells during gastrulation (Kurth and Hausen, 2000; Lee and Harland, 2010) and neurulation (Löfberg, 1974; Schroeder, 1970). A dynamic population of villous structures is present on epithelial cells during cellularization in *Drosophila*, and endocytic retraction of these structures culminates in apical cell flattening in *Drosophila* (Fabrowski et al., 2013). We thus asked whether membrane protrusions play a role in *Lrp2*-mediated AC. In mouse embryos at E8.5 (seven somites), neuroepithelial cells mostly harbored microvilli-like filamentous protrusions in both wild-type controls and LRP2-deficient embryos (Fig. 4A,B). During the next few hours of development, filamentous protrusions progressively receded in wild-type embryos and multiple bleb-like protrusions formed instead (Fig. 4C). In *Lrp2*^{-/-} embryos, cells failed to retract their filamentous protrusions (Fig. 4D), reminiscent of a failure to retract villous structures in endocytosis-deficient *Drosophila* embryos (Fabrowski et al., 2013). Indeed, endocytosis was impaired upon *Lrp2* deficiency, as morphant cells with large apical

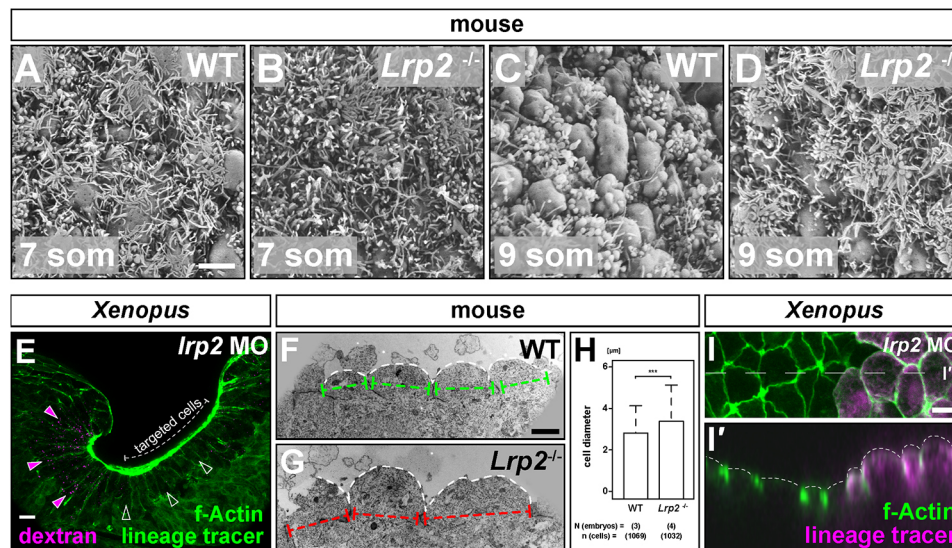


Fig. 4. No efficient remodeling of the apical surface in cells with apical constriction failure. (A-D) Scanning electron micrographs of mouse neuroepithelial cells at E8.5. Prominent filamentous, microvilli-like protrusions were present on wild-type (WT; A) and LRP2-deficient (*Lrp2*^{-/-}; B) cells at the 7-somite (som) stage. Reduced filamentous protrusions are seen at the 9-somite stage in the wild type (C), but are persistent in *Lrp2*^{-/-} (D). (E) Transverse section of *Xenopus* forebrain area at stage 19; *lrp2* morpholino oligomer (MO)-positive cells are identified by their enlarged apical surface and by cytosolic lineage tracer fluorescence. Embryos were incubated in fluorescent dextran from stages 14 to 19. Signal is present in constricted cells (filled arrowheads) but absent from MO-targeted cells (empty arrowheads). F-actin staining indicates cell borders. (F,G) Transmission electron micrographs of E9.5 coronal ultrathin sections. Normal apical cell diameters (green lines) and moderate bulging are present in the wild type (F); increased cell diameter (red lines) and excessive bulging are found in *Lrp2*^{-/-} cells (G). (H) Quantification and statistical analysis of cell diameters. Student's *t*-test. Data are mean±s.e.m. (I) En face view of neural plate showing apically enlarged *lrp2* MO-targeted cells (lineage tracer⁺) bulged outwards, see orthogonal view (I'; optical section at level indicated in I). Scale bars: 2 μm in A-D; 20 μm in E; 2 μm in F,G; 10 μm in I.

surfaces failed to take up fluorescently labeled dextran from the medium, which was readily found intracellularly in uninjected control cells (Fig. 4E). At E9.5, we noticed strong outward bulging in cells with bigger apical diameters in *Lrp2*^{-/-} embryos when compared with wild-type controls (Fig. 4F-H), and similar outward bulging in *Lrp2*-deficient *Xenopus* NP cells (Fig. 4I,I'), indicating that removal of excess apical membrane had ultimately failed. These data suggest that *Lrp2* acts as an endocytic receptor involved in eliminating surplus apical membrane, a prerequisite for efficient AC.

Impaired planar cell polarity caused by loss of *Lrp2* function

In addition to the impairment in hingepoint formation, the caudal NP remained wide and short upon *lrp2* loss of function in *Xenopus* (Fig. 2I,J). Narrowing and lengthening are hallmarks of caudal neurulation, a consequence of convergent extension (CE) movements mediated by PCP signaling (Sutherland et al., 2020). We thus asked whether cell polarity was affected upon *lrp2* loss of function. In *Xenopus*, asymmetric apical membrane localization of the core PCP component Vangl2 delineates regions undergoing CE. Already at early neurula stages (stage 13/14), Vangl2 localizes asymmetrically in NP cells at the hindbrain/spinal cord level (Ossipova et al., 2015b), which starts to be prominently narrowed by CE, although it is barely detectable in the forebrain region, which remains wide and does not converge during early stage neurulation.

We observed a regionally and subcellularly distinct distribution of pigment granules in NP cells up to mid-neurula stages (stage 15/16; Fig. S4A), which matched the localization of Vangl2 shown by Ossipova et al. (2015b). Although in the forebrain region, pigment was distributed symmetrically throughout individual cells (Fig. S4A,A'), it was asymmetrically distributed in cells caudal to the mid-hindbrain level (Fig. S4A,A'). In *lrp2* morphants, in which the NP remained widened on the injected side (Fig. 5A,B),

asymmetry at the hindbrain level was disrupted, as pigment granules distributed evenly along the cell periphery (Fig. 5B₁,B₁',B₁''), indicating that *Lrp2* was required for planar polarity of NP cells at early/mid-neurula stages. Localization of *Lrp2* itself shifted from the enrichment seen in constricting cells at early/mid-neurulation (stage 15; compare with Fig. 1B) to an asymmetric localization towards the medio-anterior aspect of single cells at stage 16 (Fig. 5C,C',C'_{1,2}).

At mid- to late neurula stages, the forebrain area narrows, leading to rapid convergence of the anterior neural folds. This suggests that planar asymmetry of PCP components plays a role in the forebrain area from mid- to late neurula stages onwards. To test whether this process is influenced by *Lrp2*, we first assessed the dynamics of Vangl2 localization in the forebrain area at mid- to late neurula stages. Low doses (to avoid a gain of function phenotype) of *eYFP-vangl2* were injected into the neural lineage and detected using an anti-GFP antibody (Fig. 5D; Fig. S4B,C). A temporally dynamic pattern of Vangl2 subcellular localization was observed in the forebrain region. In embryos at stage 16 or earlier, Vangl2 was restricted to the cytoplasm and localized subapically in vesicular structures (Fig. 5D'-D''; Fig. S4B), where it frequently abutted or overlapped with *Lrp2*-positive vesicles (Fig. S4C). From stage 17 onwards, cytoplasmic Vangl2 disappeared and re-distributed to the membrane (Fig. S4D,E). During this dynamic process, instances of *Lrp2* and Vangl2 overlap at the membrane were observed (Fig. S4D,D'), but the two proteins were mostly non-overlapping. Vangl2 also started to show an asymmetric localization towards the medio-anterior aspect of individual cells (Fig. S4E,E',E'_{1,2}). As re-localization of *Lrp2* appeared slightly earlier (stage 16) than Vangl2 redistribution (stage 17), we were prompted to test whether *Lrp2* was required for the localization of Vangl2 in the forebrain region. When *eYFP-Vangl2* was co-injected with *lrp2* MO (Fig. 5E)

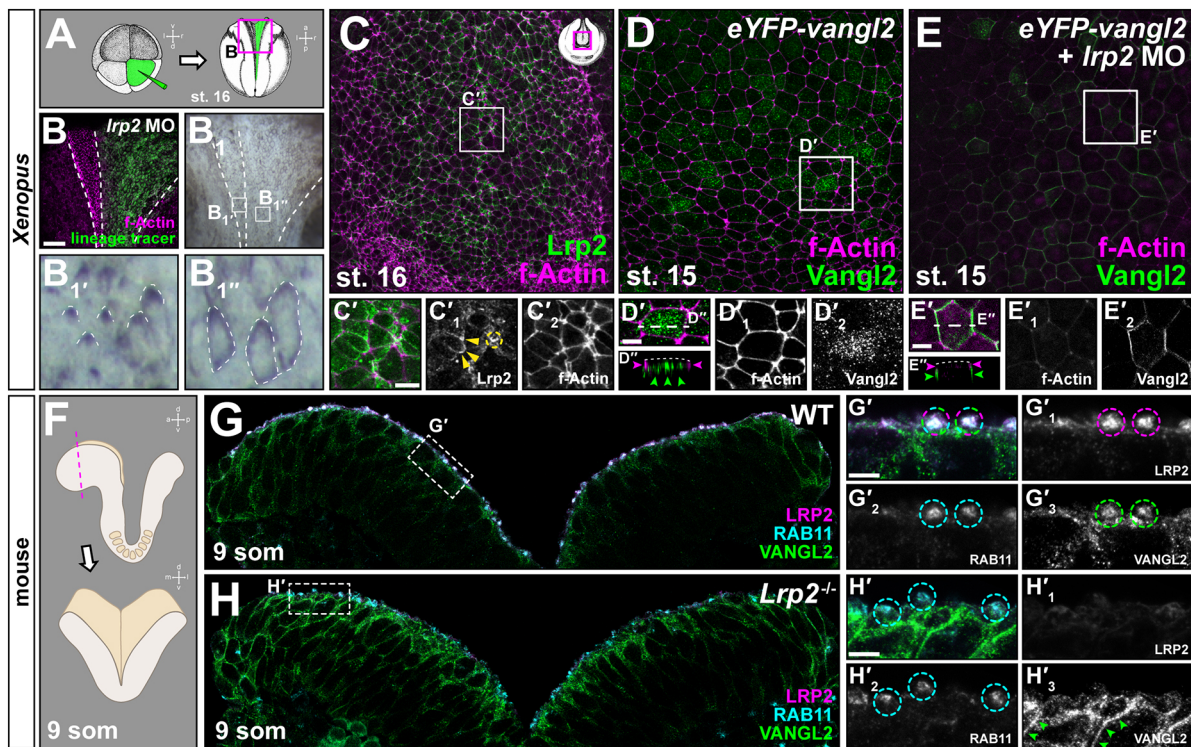


Fig. 5. Lrp2 is required for planar cell polarity and regulates subcellular localization of Vangl2. Analysis of planar cell polarity in embryos en face (A-E) and on sections (F-H). (A) Scheme for injection of morpholino oligomer (MO) targeting *lrp2*; area for analysis at stage (st.) 16 in B is indicated by a box. (B) Dorsal view of mid-/hindbrain area; the width of the neural plate is greater on the injected side, F-actin delineates cell borders. (B₁) Bright-field image of same embryo shows pigment granule localization towards the anterior in uninjected control cells (B₁); circumferential distribution is seen in apically wide morphant cells (B₁). (C) Beginning of asymmetric Lrp2 distribution; F-actin delineates cell borders. (C') Magnification of area indicated in C; there is medio-anterior distribution of Lrp2 (arrowheads in C'₁), which is also seen in apically constricted cells (circle in C'₁). (C'₂) F-actin single channel. (D,E) *eYFP-vangl2* injected into the A1 lineage in 4- to 8-cell embryos, detected at stage 15 using immunofluorescence for GFP and F-actin staining. Dotted pattern of *eYFP-Vangl2* expression (6/6 embryos; D,D'; magnification of inset in D), which is located subapically in vesicle-like structures (green arrowheads in D'; optical section indicated in D'; magenta arrowheads indicate f-Actin belt). Upon *lrp2* MO injection, Vangl2 localized at cell borders (7/9 embryos, two independent experiments; E,E') and subapically in the basolateral membrane (green arrowheads in E', optical section as indicated in E'; magenta arrowheads indicate f-Actin belt). (D'₁,D'₂,E'₁,E'₂) Single channels. (F) Schematic illustrating the level of transverse sections in G,H. (G,H) LRP2 and VANGL2 distribution at the 9-somite stage. (G',G'₁₋₃,H',H'₁₋₃) Higher magnifications of the areas indicated by the boxes in G,H, and single channels thereof. Apical colocalization (dashed circles) of LRP2 and VANGL2 in RAB11-positive compartments occurs in wild type (WT; G,G') compared with absence of VANGL2 from RAB11-positive compartments in *Lrp2*^{-/-} cells (H,H'); arrowheads in H'₃ indicate relocalization of VANGL2 to the basolateral membrane. l, left; p, posterior; r, right; v, ventral. Scale bars: 100 μm in B; 10 μm in C',D',E'; 5 μm in G',H'.

and analyzed at stage 15 (i.e. before Vangl2 re-distribution occurred in controls), we observed that Vangl2 was shifted to the lateral cell membranes and localized subapically, basal to the apical actin ring (Fig. 5E'-E'').

LRP2 was similarly required for correct VANGL2 distribution in the mouse NP (Fig. 5G,H). In wild-type samples, LRP2 colocalized with VANGL2 in condensed apical structures, which were identified as recycling endosomes by RAB11 immunoreactivity (Fig. 5G,G',G'₁₋₃). Although in wild-type controls, only small amounts of VANGL2 were found intracellularly in vesicular structures (Fig. 5G',G'₃), in receptor mutant NP cells (Fig. 5H,H',H'₁₋₃), VANGL2 predominantly localized to basolateral membrane domains (arrowheads in Fig. 5H'₃) but hardly at the apical surface.

Misexpression and -localization of core PCP proteins affects cell polarity and directional movement of cells, impairing, for example, CE movements in the posterior NP (Darken et al., 2002; Goto and Keller, 2002; Wallingford et al., 2000). So far, these processes have been analyzed in the posterior neural plate, as the anterior neural plate remains wide during those stages, i.e. does not undergo CE. We thus defined descriptors of cell polarity within the tissue plane – cell long axis orientation and anisotropy – that could also be applied to the forebrain area (Fig. S4F). In wild-type *Xenopus* embryos, the

long axis of posterior neural plate cells re-orient from an anteroposterior to a mediolateral direction during posterior neural fold convergence (Butler and Wallingford, 2018). Forebrain cells at stage 15, i.e. before anterior neural fold convergence, were anisotropic with their long axis predominantly oriented in a mediolateral direction (Fig. S4G). Concomitant with anterior neural fold convergence and apical surface reduction during stages 16 and 17, anisotropy persisted but long axis orientation shifted from mediolateral to anteroposterior. However, at stage 17, *lrp2*MO-injected cells had not reduced their surface area, but showed reduced anisotropy and did not adopt a preferential planar orientation (Fig. S4H,I). Despite the failure to establish anisotropy and planar alignment, *lrp2*MO cells nevertheless underwent so-called T1 transitions, i.e. the shrinkage of a mediolaterally oriented cell-cell junction into a vertex and its resolution into an anteroposteriorly oriented junction (Fig. S4J,K). T1-transitions are one of the mechanisms driving CE and require the orchestrated shrinking and elongation of junctions (Bertet et al., 2004; Williams et al., 2014), a process that did not appear to be generally impaired by loss of Lrp2.

Together, our data from mouse and frog show that: (1) the core PCP protein Vangl2 was present in forebrain area NP cells in a

temporally dynamic fashion, shifting its subcellular localization from apical recycling endosomes to basolateral membrane, concomitant with convergence movements in the forebrain area; (2) LRP2 colocalized with VANGL2 in apical recycling endosomes; and (3) Lrp2/LRP2 was required to prevent the premature redistribution of Vangl2 from apical recycling endosomes to basolateral membrane, which (4) coincided with impaired cell polarity but did not overtly affect cell neighbor exchange.

Lrp2 interacts with intracellular adaptors to mediate cell shape changes

The endocytic pathways of transmembrane proteins are directed by intracellular adaptors. This led us to ask how Lrp2 function is mediated intracellularly. Shroom3 acts as an intracellular adaptor and scaffold protein. It binds actin, induces AC and is crucial for NP folding in both mouse and frog (Haigo et al., 2003; Hildebrand and Soriano, 1999). In the *Xenopus* NP, *shroom3* is expressed in cells engaged in AC (Haigo et al., 2003). We found that Lrp2 accumulated in apically constricted hinge point cells (Fig. 6A, A_{1,2}), although it was not enriched in cells in which AC had been inhibited by MO-mediated *shroom3* loss of function (Fig. 6A, A_{1,2}). Likewise, Lrp2 accumulated apically in cells of *Xenopus* blastula stage embryos, in which AC had been induced ectopically by injection of *shroom3-myc* (Fig. 6B, B_{1,2}; Haigo et al., 2003), indicating that Lrp2 was recruited to sites of *shroom3*-dependent AC. We then asked whether *shroom3*-mediated AC depends on the presence of Lrp2. In cells of the animal hemisphere, *shroom3*-induced ectopic AC manifests as excessive accumulation of pigment during blastula/gastrula stages (Haigo et al., 2003). Although *shroom3-myc* efficiently induced strong ectopic AC (Fig. 6C,F), loss of *lrp2* did not entirely abrogate constriction, but significantly decreased the grade of pigment accumulation (Fig. 6D,F). Re-introduction of *lrp2* rescued the MO effect (Fig. 6E,F), indicating that the modulation of AC was specific to *lrp2* loss of function. These data show functional interaction of the endocytic receptor Lrp2 and the constriction-inducing scaffold protein Shroom3 at the apical surface of polarized cells to facilitate efficient AC.

NHERF1 (Slc9a3r1) and GIPC1 are known intracellular adaptors of LRP2 (Gotthardt et al., 2000; Naccache et al., 2006; Slattery

et al., 2011); however, their role in the developing neural tube has not been analyzed. NHERF1, which mediates endocytosis and trafficking of cell surface receptors, contains two PDZ domains as well as an ERM domain that enables interaction with the cytoskeleton (Weinman et al., 1998). NHERF1 overlapped with LRP2 at the apical surface of wild-type E8.5 mouse neural folds (Fig. S5A,A₁,A₂,B,B₁,B₂). Strikingly, NHERF1 was lost in *Lrp2*^{-/-} mutants (Fig. S5C,C₁,C₂,D,D₁,D₂), suggesting a direct interaction of NHERF1 and LRP2.

Gipc1 contains one PDZ domain and is supposed to guide endocytic vesicles through the apical actin meshwork by its interaction both with receptors and myosin 6 (Aschenbrenner et al., 2003; Naccache et al., 2006). Gipc1 was localized in the NP of both mouse and *Xenopus* (Fig. 7A-C). In the mouse anterior NP at E8.5 (seven somites), GIPC1 localization showed a clear gradient: it was high in dorsolateral areas with large cell surfaces (Fig. 7A,A_{1,2},A_{1'2'}) and lower where extensive AC occurred, such as in the midline and OE (Fig. 7A,A_{1,2},A_{1'2'}). Similarly, in *Xenopus*, Gipc1 was absent in highly constricted cells at the border of the NP (Fig. 7B,B'), which give rise to the OE (compare with Fig. 3A). In single constricted cells located close to the NP border, Gipc1 signal was condensed subcellularly (Fig. 7C'''), indicating that AC correlated with localized accumulation and disappearance of Gipc1 towards the NP border, suggestive of its degradation. At the tissue level, expression levels of GIPC1 and LRP2 were almost inversely correlated in the mouse. In the OE, where low levels of Gipc1 were found, Lrp2 was enriched (Fig. 1B,C; Fig. 7A₁,A_{1'},A₃,A_{3'}). In agreement with the findings in mouse, in *Xenopus*, the expression levels of Gipc1 and Lrp2 did not generally correlate (Fig. 7C, compare C'₁,C'₂ and C''₁,C''₂). However, at the cellular level, colocalization was frequently found, both in large and in constricted cells (Fig. 7C''',C''''), suggesting a spatially and temporally dynamic interaction between the two proteins.

To functionally analyze *gipc1*, a previously validated MO was used (Tan et al., 2001) that also induced a specific, i.e. rescuable, phenotype in the NP (Fig. S5E-I,E'-H'). Similar to the phenotype of *lrp2* morphants, MO-mediated *gipc1* loss of function resulted in larger apical cell surfaces, indicating that Gipc1 also mediated AC (Fig. S5G,I). Having confirmed that both proteins were required for AC, we tested whether they functionally interacted in the process.

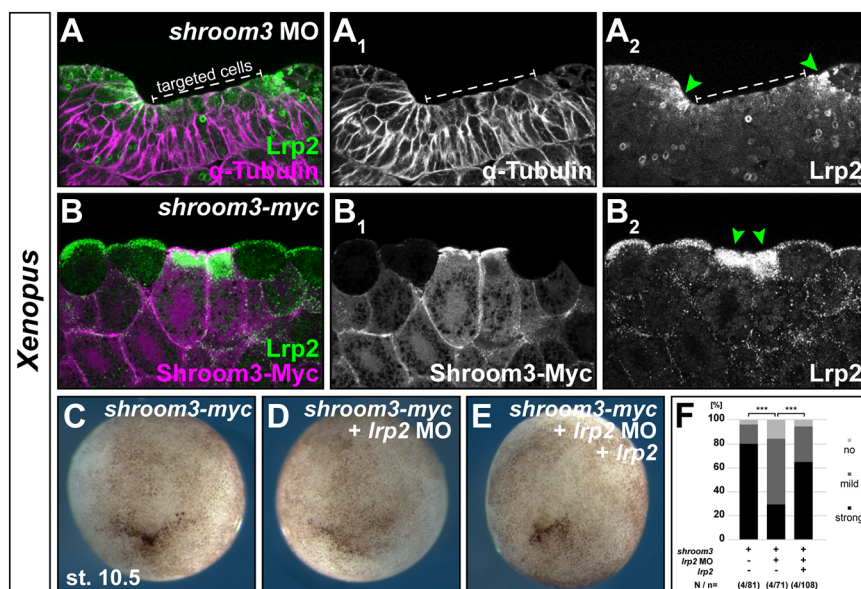


Fig. 6. *lrp2* functionally interacts with *shroom3* in mediating apical constriction. (A) Transverse section through neural plate; unilateral injection of *shroom3* morpholino oligomer (MO) produces a failure of apical constriction (α -tubulin highlights wide cell surfaces; A₁); apical Lrp2 accumulation in constricting hinge point cells (arrowheads in A₂) and lack of apical Lrp2 recruitment in targeted cells. (B) Section through animal cap; ectopic apical constriction is induced in cells injected with *shroom3-myc* (detected by anti-Myc antibody; B₁) coinciding with apical Lrp2 accumulation (arrowheads in B₂). (C-E) *shroom3*-induced ectopic apical constriction in animal cap cells at stage (st.) 10.5 (C) is abrogated by co-injection of *lrp2* MO (D) and restored by co-injection of *lrp2*. (F) Quantification and statistical analysis of experiments in C-E: no, mild or strong ectopic constriction are quantified. *N*=number of experiments; *n*=number of embryos, χ^2 test.

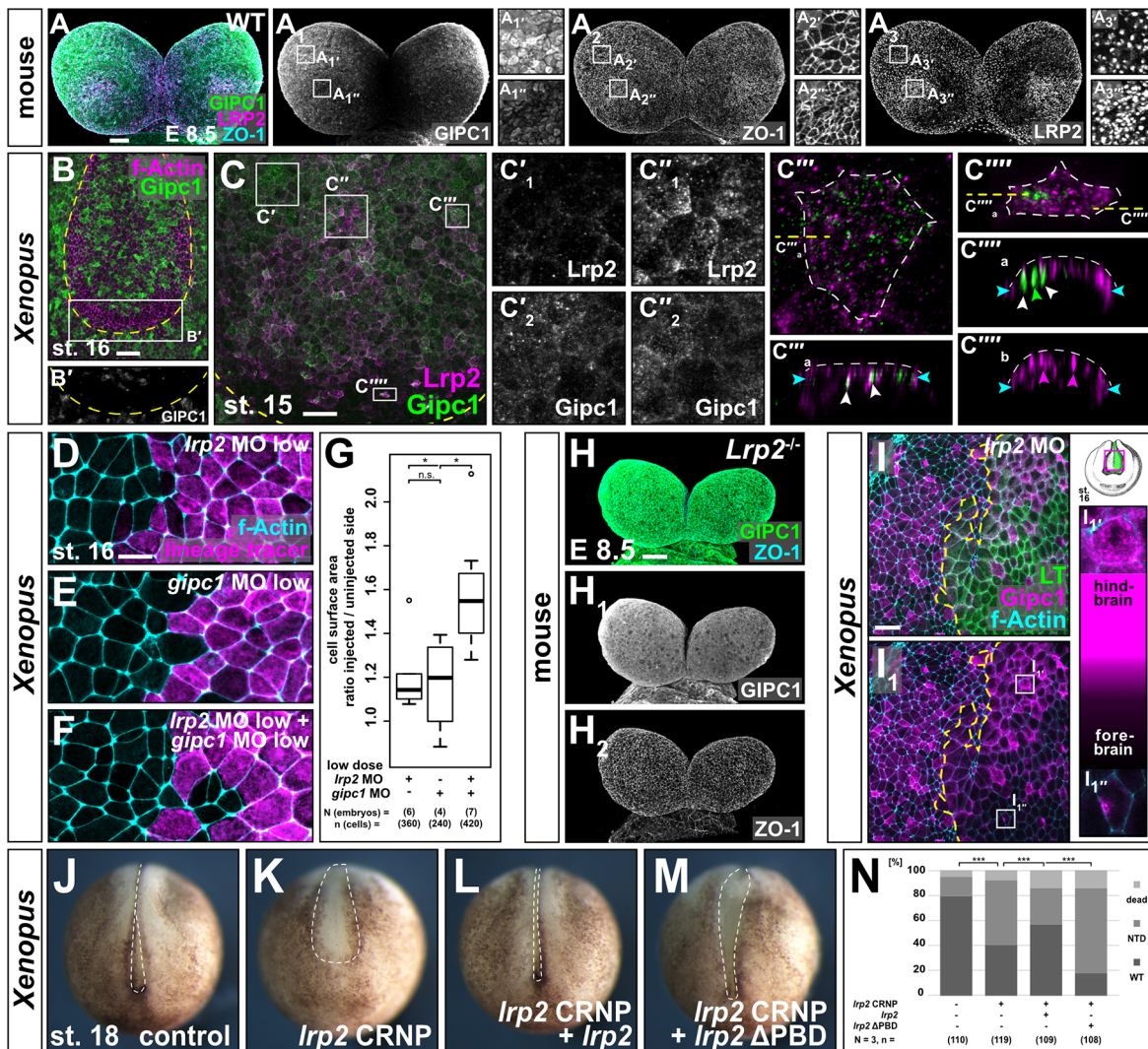


Fig. 7. Lrp2 mediates apical constriction by functional interaction with Gipc1. (A) Frontal view of wild-type (WT) mouse forebrain area at E8.5 (7 somites). Immunofluorescence (IF) staining reveals localization of GIPC1 and LRP2; ZO-1 marks cell borders. (A₁-A₃) Single channels. (A₁'-A₃') Magnification of areas indicated in A₁-A₃; differential GIPC1 intensities exist between large and constricted cells. (B,C) Frontal views of stage (st.) 16 (B) and stage 15 (C) embryos; dashed line indicates the anterior limit of the neural plate; immunofluorescence reveals the spatially dynamic localization of Gipc1 (B) and spatially dynamic colocalization of Lrp2 and Gipc1 (C). (B') Single channel of Gipc1; higher magnification of the area indicated in B. Boxed areas indicated in C are shown at higher magnification in C'-C'''. (C'₁, C'₁', C'₂, C'₂') Single channels. Gipc1 is present in areas with low (C'₁, C'₂') or high (C''₁, C''₂') amounts of Lrp2. Dispersed distribution of Lrp2 and Gipc1 in a cell with a large apical surface (C'''), also visible in an orthogonal optical section (C''''_a); indicated in C''''; sites of Lrp2/Gipc1 co-localization are indicated (white arrowheads). (C''''_a) Cell with a constricted surface showing Gipc1 accumulation. (C''''_a, C''''_b) Colocalization (white arrowheads) or separate localization (green or magenta arrowheads) are indicated. Blue arrowheads indicate the level of circumferential actin; dashed line indicates apical surface in C''''_a, C''''_b. (D-F) Functional interaction of Lrp2 and Gipc1 demonstrated by individual (D,E) or combined (F) injection of low-dose *lrp2/gipc1* morpholino oligomer (MO); targeted cells with lineage tracer (LT) fluorescence are shown. (G) Graphical representation of results from D-F; box plot and Wilcoxon rank sum test. (H) Frontal view of LRP2-deficient (*Lrp2*^{-/-}) mouse forebrain area at E8.5 (seven somites). Immunofluorescence reveals localization of Gipc1; ZO-1 outlines cells. (H₁, H₂) Single channels. There is homogenous GIPC1 signal throughout the neuroepithelium. (I) Mislocalization of Gipc1 in *lrp2* MO-injected cells in stage 16 embryos; the magnified forebrain area is marked by a box in the schematic. Targeted cells are identified by LT; dashed line delineates targeted/non-targeted areas. (I₁) Without LT. (I₁', I₁') Higher magnification of single cells indicated by the boxes in I₁; Gipc1 increases in hindbrain and decreases in the forebrain area. (J-M) Embryos for CRISPR/Cas9 experiments selected at the one-cell stage and incubated until uninjected controls (J) reached stage 18/19. (K) Injection of Cas9 ribonucleic particles (CRNP) containing sgRNA1. (L,M) Co-injection of CRNP together with the *lrp2* construct (L) or with *lrp2* ΔPBD (M). (N) Graphical representation of results from J-M, χ^2 test. Cell borders in D-F, I are visualized using F-actin staining. Scale bars: 50 μ m in A, C, H, I; 100 μ m in B; 20 μ m in D-F.

To do this, *lrp2* or *gipc1* MOs were injected in doses low enough to induce no or only very mild AC phenotypes (Fig. 7D-G). Low dose *lrp2* or *gipc1* MO increased the median cell surface area by 14% or 20%, respectively (Fig. 7D,E,G), while injection of both low dose MOs led to an increase in median cell surface area of 55% (Fig. 7F,G). As the actual increase was higher than expected for an additive effect (55% versus 34% expected), it suggested that *lrp2*

and *gipc1* acted epistatically in the process of AC. Consistent with its described role in PCP (Giese et al., 2012), *gipc1* loss also affected Vangl2 expression. While Vangl2 was prematurely mislocalized to the membrane in *lrp2* morphants, *gipc1* MO injection led to an overall decrease in Vangl2, with the protein mostly depleted from vesicular structures and little remaining at the plasma membrane (Fig. S5J,J').

lrp2 loss of function also altered the distribution of Gipc1 in both mouse and frog. In the forebrain area of *Lrp2*^{-/-} mice, LRP2 deficiency completely abolished the GIPC1 expression gradient found in the wild type (Fig. 7H; compare with Fig. 7A₁), leaving all cells with a high level of GIPC1, comparable with that of GIPC1 in wild-type cells with a large apical surface (compare with Fig. 7A₁). In the forebrain area of *Xenopus lrp2* morphants, Gipc1 disappeared and only spots of asymmetrically localized Gipc1 accumulation within single cells remained (Fig. 7I₁). In the hindbrain/spinal cord area, on the contrary, Gipc1 did not disappear, but was in fact upregulated (compare Fig. 7I₁ with 7I₁’).

As Gipc1 has been described to bind to the C-terminal PBD of Lrp2 (Naccache et al., 2006), we asked whether this motif was required for Lrp2 function during NTC. Embryos at the one-cell stage were injected with CRNP containing sgRNA1 (compare with Fig. S2D), which significantly induced aberrant NTC compared with uninjected controls (Fig. 7J,K,N). Co-injection of CRNP and *lrp2* (carrying the wild-type cytoplasmic domain) significantly reduced the amount of embryos with NTDs (Fig. 7L,N). Injecting CRNP together with *lrp2* ΔPBD, a construct lacking the last four amino acids, which constitute the distal PBD, not only failed to rescue but also increased the number of embryos with NTDs (Fig. 7M,N), which primarily manifested as widening and tissue disintegration in the caudal region of the NP. Together, these data show novel functional interactions of Lrp2 with the intracellular adaptor proteins Shroom3, NHERF1 and Gipc1, suggesting that spatially and temporally coordinated interaction of Lrp2 with several intracellular adaptors mediates neural morphogenesis.

DISCUSSION

Our functional analysis of mouse and *Xenopus* neurulation identified a conserved function of Lrp2 as a regulator of NTC. Lrp2 acted in orchestrating AC and PCP-mediated CE, two morphogenetic processes essential for proper NTC in vertebrate model organisms, as well as humans (Copp et al., 2003; Wallingford et al., 2013).

Lrp2 and its endocytic activity enable efficient apical constriction

As suggested by its accumulation in constricting cells of the NP, Lrp2 was required cell-autonomously for AC. The spatially controlled AC of neural tissue creates hinge points/hinges and the longitudinal folding of neural tissue (Colas and Schoenwolf, 2001). Impairment of AC and hinge point formation has been clearly linked to anterior NTDs (Wallingford, 2005).

How does Lrp2 as an endocytic receptor contribute to AC? Evidence is accumulating that efficient AC relies on a dual mechanism, i.e. mechanical constriction of the apical surface by actomyosin interaction accompanied by the removal of apical membrane via endocytosis (Fig. 8; Lee and Harland, 2010; Miao et al., 2019; Ossipova et al., 2015a, 2014). In addition, AC in the NP takes place in a pulsatile manner with incremental constriction (Christodoulou and Skourides, 2015), reminiscent of a ‘ratchet’ mechanism (Martin and Goldstein, 2014; Martin et al., 2009). During ratcheting, cell surface decrease is followed by a stabilization phase – a cyclic process, repeated until the surface is maximally constricted (Fig. 8). Removal of surplus membrane may be the mechanism underlying cell surface area stabilization (Miao et al., 2019). Our observations suggest that loss of Lrp2 does not interfere with actomyosin activation and mechanical induction of constriction. This is supported by the finding that *lrp2* loss of function never entirely suppressed Shroom3-induced AC and is

consistent with the lack of change in actin dynamics upon loss of Lrp2. We postulate that Lrp2 enables efficient AC by remodeling the apical membrane via endocytosis to stabilize apical surface shrinkage between cycles of actomyosin constriction. This endocytic function is supported by: (1) the finding that LRP2 localized to the ciliary pocket at the base of the primary cilium, a highly endocytic plasma membrane domain (Benmerah, 2013; Molla-Herman et al., 2010); (2) the severe inhibition of dextran endocytosis upon *lrp2* loss of function; and (3) the formation of membrane protrusions that were not removed from the constricting surface in a timely manner.

In addition to membrane removal, ligand uptake by LRP2 can also be relevant for AC. One physiological ligand for LRP2 in the neural plate is folate bound to its receptor FOLR1 (Kur et al., 2014). FOLR1 is required for AC and consequently for neurulation in *Xenopus* (Balashova et al., 2017), and acts on actomyosin-dependent AC alongside Shroom3 (Martin et al., 2019). At this point, the LRP2-mediated membrane removal identified here and folate-dependent intracellular processes might very well interact.

Lrp2 controls the timing of PCP protein localization

It has been shown that endocytic uptake, recycling, intracellular re-localization and endocytic removal of uncomplexed PCP proteins at cell junctions are essential processes for establishing PCP-mediated cell and tissue polarization (Eaton and Martin-Belmonte, 2014). Acquisition of cell polarity brought about by endocytic trafficking is thus a temporally dynamic process, illustrated, for example, by Vangl2 localization. In zebrafish dorsal mesoderm, Vangl2 is first detected cytoplasmically in vesicle-like structures and relocates to the membrane shortly before the onset of PCP-dependent cell polarization (Roszko et al., 2015). It accumulates asymmetrically just before initiation of CE. The temporal differences in wild-type Vangl2 localization prior to and during convergence of the *Xenopus* neural folds that were observed here match the dynamics in zebrafish mesoderm. This timeline suggests that the finalization of forebrain NTC requires the temporal control of PCP. A requirement for endocytosis in this process is underlined by our finding that loss of Lrp2 induced a premature and aberrant relocalization of Vangl2 from apical cytoplasmic compartments (Rab11-positive recycling endosomes) to basolateral membrane in mouse and frog. Interestingly, despite a localization to the basolateral membrane, Vangl2 did not accumulate in a planar polarized fashion. This suggests that the correct succession of events during PCP-dependent neural fold convergence requires Lrp2-mediated endocytic trafficking: (1) for the temporal restriction of Vangl2 to cytoplasmic vesicular compartments; and (2) to control the levels and asymmetric distribution of PCP proteins in the subapical/basal membrane. The latter is in line with the phenotype of PCP protein gain of function, which also disrupts convergence movements and cell polarity (Darken et al., 2002; Goto and Keller, 2002; Wallingford et al., 2000). We conclude that Lrp2-mediated endocytosis and trafficking are required for the precise control of timing, amount and localization of PCP proteins to drive anterior neurulation.

Lrp2 as a hub to orchestrate AC and PCP?

A functional link between AC and PCP, especially during neural tube closure, has become increasingly evident (McGreevy et al., 2015; Nishimura et al., 2012; Ossipova et al., 2014, 2015b). As we found that both morphogenetic processes were affected by *lrp2* loss of function, Lrp2-mediated endocytosis and intracellular trafficking could be a common denominator for AC and PCP. How would an

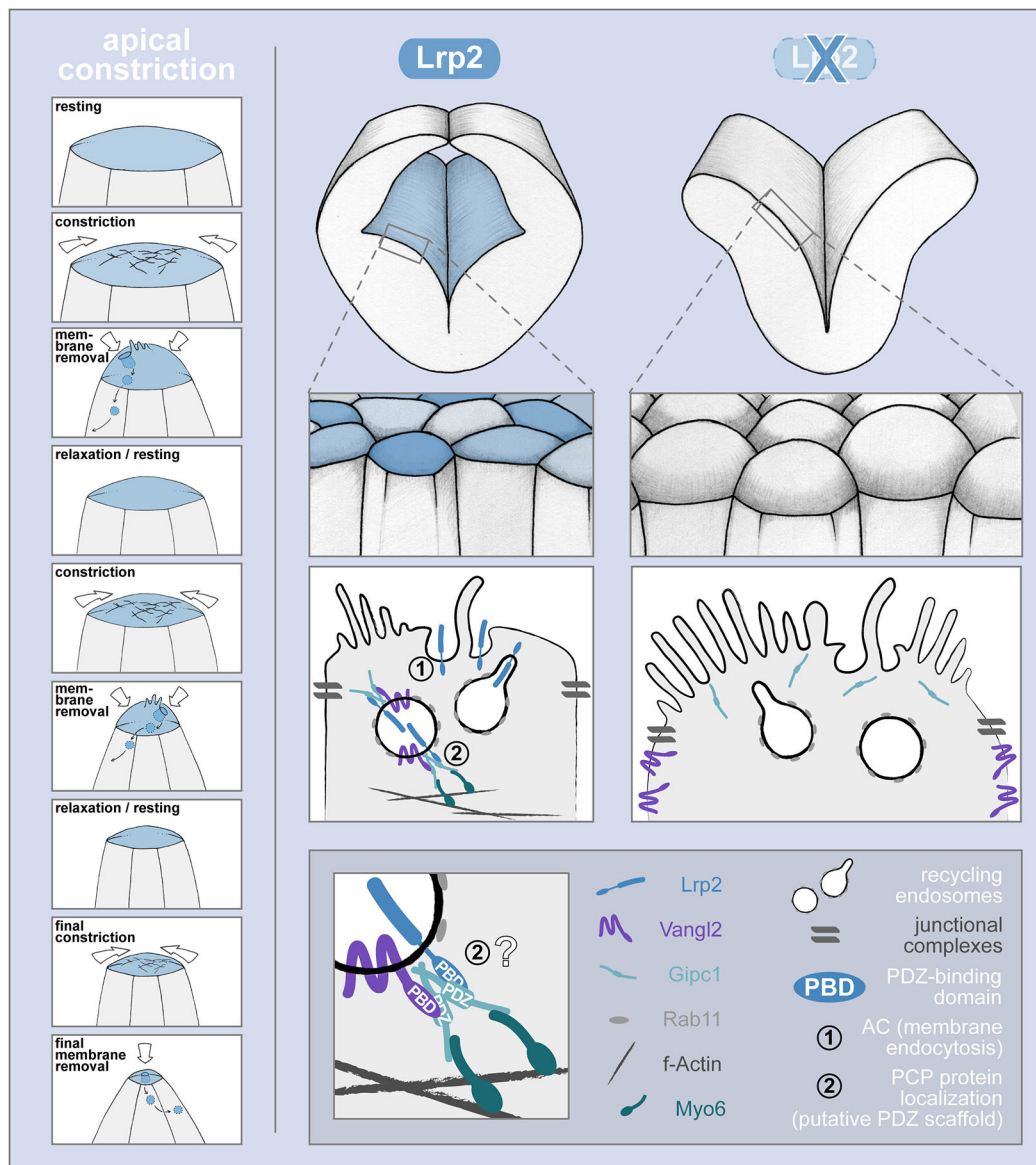


Fig. 8. Hypothetical model of Lrp2 functional interactions in neural tube closure. Apical constriction is seen as a stepwise process with repetitive modules of actomyosin-mediated constriction and Lrp2-mediated membrane removal (left column). Apical constriction of Lrp2-positive neuroepithelial cells facilitates neural tube closure (middle column). Lrp2 mediates endocytic removal of apical membrane (1) as well as correct temporospatial localization of Vangl2 (2) via recycling endosomes. The Lrp2/Vangl2 interaction is likely facilitated by PDZ/PBD-mediated intracellular scaffolding via dimerized Gipc1, connecting to Myo6 and the actin cytoskeleton. Lack of Lrp2 (right column) entails defective neural tube closure due to impaired apical constriction. Removal of apical membrane fails and proper subcellular sorting of Vangl2 and Gipc1 is disturbed, leading to their mislocalization.

interaction between AC and PCP – each with a conspicuously different cellular outcome – be mediated by a single receptor? A likely explanation lies in the ability of Lrp2 to differentially interact with intracellular adaptors and scaffold proteins via its C-terminal cytoplasmic motifs.

Shroom3 is an intracellular adaptor and scaffold protein. We found that Lrp2 was recruited apically upon *shroom3* injection and was required for efficient Shroom3-induced AC. It remains to be tested whether a scaffold containing Lrp2 and Shroom3 is necessary for initiation of endocytosis, intracellular trafficking and efficient AC. Protein scaffolds also serve as integrators for signaling pathways and for compartmentalization of components that contribute to different pathways at different times (Pawson and Scott, 2010). A Lrp2-based scaffold might thus serve as a platform for temporospatial integration of AC and PCP (Fig. 8). Both Lrp2

and Shroom3 feature a conserved PBD [X(S/T)X(V/L)] for class I PDZ domains in their distal C-termini. While the Shroom3 PBD remains to be functionally analyzed (Haigo et al., 2003; Hildebrand and Soriano, 1999; Lee et al., 2007), the Lrp2 PBD is functionally relevant for interaction with the class I PDZ domain-containing adaptor protein Gipc1 (Naccache et al., 2006). As Gipc1 also dimerizes (Reed et al., 2005), it serves as a connector and may create an AC-mediating scaffold containing Lrp2, Shroom3 and Gipc1. Indeed, we demonstrate here a novel requirement for Gipc1 in facilitating AC and NTC. Lrp2-Gipc1 functional interaction is supported by the loss-of-function phenocopy of *lrp2* and *gipc1*, their epistatic relationship and the requirement for the PBD of Lrp2 in rescue experiments. The influence of Lrp2 on Gipc1 localization further suggests not only a functional, but also a physical, interaction between these proteins. We could thus envision a

complex of Shroom3, Lrp2 and Gipc1 that facilitates efficient AC via engagement of actomyosin (Shroom3) and endocytic elimination of membrane (Lrp2). Indeed, Gipc1 dimers interact with Lrp2 and at the same time mediate the formation of a complex with myosin 6, which facilitates the trafficking of endocytic vesicles through the apical actin network (Aschenbrenner et al., 2003). Thus, Gipc1-mediated guidance of Lrp2-positive endocytic vesicles through the apical actin meshwork could account for efficient removal of apical membrane upon Shroom3-induced AC in anterior NP cells. In such a setting, the pathways of Lrp2-mediated endocytosis and Shroom3-mediated actomyosin recruitment cooperate to integrate processes that are crucial for AC.

Our observations here suggest that a phase of Shroom3-initiated AC during early anterior neurulation is succeeded by PCP-mediated CE to finalize anterior NTC. Such a temporal succession of AC and PCP in the forebrain area could also be mediated through scaffolding by Gipc1 (Fig. 8). Gipc1 is clearly also involved in the establishment of PCP. It directs the localization of the core PCP protein Vangl2 and its loss of function elicits PCP phenotypes (Giese et al., 2012). Vangl2, in turn, is known to localize differentially in phases of AC versus PCP. It is recruited to the apical membrane in constricting cells *in vivo* and upon ectopically induced AC (Ossipova et al., 2014, 2015a). Our temporal analysis of Vangl2 localization in the anterior NP of *Xenopus* revealed that the apical vesicular localization of Vangl2 coincided with AC, while membrane localization occurred later during neural fold convergence. This temporal pattern and the premature membrane mislocalization of Vangl2 upon *lrp2* loss of function suggests that Lrp2 is required to retain Vangl2 in recycling endosomes during AC. Its controlled release from recycling endosomes would enable its relocalization to the membrane and the initiation of PCP/CE. As Gipc1 can bind to both Lrp2 and Vangl2, it could act as an adaptor between both proteins and mediate the controlled release of Vangl2 from the recycling route. We propose that AC and PCP/CE in the anterior NP are temporally and spatially separated processes, the succession of which is regulated by Lrp2/Gipc1-mediated endocytosis and intracellular trafficking.

Conservation of Lrp2 function in disease etiology

The clinical presentation of individuals with *LRP2* gene mutations are also present in the *LRP2*-deficient mouse models (Cases et al., 2015; Hammes et al., 2005; Kur et al., 2014; Sabatino et al., 2017; Spoelgen et al., 2005; Wicher and Aldskogius, 2008). Our report demonstrates that *Xenopus* is a new valuable model for the functional analysis of Lrp2 deficiency. In addition to the matching neural localization and loss-of-function phenotypes between mouse and frog, *Xenopus lrp2* is expressed in DBS disease manifestation sites such as otic vesicle and pronephros (Fig. S1; Christensen et al., 2008). This suggests that the frog will also be highly valuable for studies on human *LRP2*-related congenital disorders of organs other than the neural tube. Of note, the intracellular adaptors addressed here indeed share similar loss-of-function phenotypes such as kidney insufficiency [Shroom3 (Khalili et al., 2016), NHERF1 (Shenolikar et al., 2002) and Gipc1 (Naccache et al., 2006)] and hearing loss [NHERF1 (Giroto et al., 2019) and Gipc1 (Giese et al., 2012)].

Together, our data suggest a novel role for *LRP2* in the functional interaction with subapical scaffolds that are essential for proper neuroepithelial morphogenesis and neural tube closure. Our findings here support the notion that the function of Lrp2 in these processes is conserved also in humans. Thus, combining the power of the *Xenopus* and mouse embryological models should

prove highly valuable to studying the mechanistic origins of human NTDs and other congenital disorders related to *LRP2* dysfunction.

MATERIALS AND METHODS

Animals

Mouse

Animal experiments were performed according to institutional guidelines following approval by local authorities (X9005/12). Mice were housed in a 12 h light-dark cycle with *ad libitum* food and water. The generation of mice with targeted disruption of the *Lrp2* gene on a C57BL/6NCr1 background has been described previously (Willnow et al., 1996). Analyses of embryonic neural tube defects were carried out in *LRP2*-deficient and in somite-matched wild-type and heterozygous littermates on a C57BL/6NCr1 background. *Lrp2*^{-/-} embryos at E8.5, i.e. before neural tube closure, were included in the studies in an unbiased way and not preselected by phenotypic appearance.

Xenopus

All animals were treated according to the German regulations and laws for care and handling of research animals, and experimental manipulations were approved by the Regional Government Stuttgart, Germany (Vorhaben 'Xenopus Embryonen in der Forschung' V340/17 ZO and V349/18 ZO).

Cloning of expression constructs

The constructs here referred to as *lrp2* and *lrp2*ΔPBD (lacking the last four amino acids that constitute the PDZ-binding domain, PBD) were generated from HA-Meg4, encoding an extracellularly truncated human megalin/*LRP2* (kindly provided by Maria Paz Marzolo, Pontificia Universidad Católica de Chile). HA-Meg4 contains an HA-tag N-terminally, followed by the fourth ligand-binding domain as well as the transmembrane and intracellular domains. Using a standard PCR-based approach with primers containing restriction sites, the constructs were amplified and subcloned into the pCS2+ vector.

Microinjections of morpholino oligomers and mRNA in Xenopus

Drop size was calibrated to 4 nl per injection and dextran tetramethylrhodamine or dextran Alexa Fluor 488 (MW 10,000, 0.5–1 μg/μl, Thermo Fisher Scientific) were added as a lineage tracer. Morpholino oligomers (MOs; Gene Tools) used were *lrp2* MO (ATG-spanning, translation-blocking; 5' AGTCCCCTCTCTGCTCCTGC 3') and *gipc1* MO (5'UTR-located, translation-blocking; 5' CCACGGACAGCAAATCT-CACACAG 3'; Tan et al., 2001), both 0.5–1 pmol per injection; for epistasis experiments, 0.3 pmol MO was used each. The *gipc1*, *shroom3-myc* and *eYFP-vangl2* (kindly provided by Alexandra Schambony, Friedrich-Alexander-University Erlangen, Germany) constructs contained the ORFs of *Xenopus laevis gipc1.L*, *shroom3.L* and *vangl2.S*, respectively. Capped mRNAs were synthesized using mMessage mMachine (Ambion); amounts per injection were: *gipc1*, 10–30 pg; *lrp2*, 400 pg; *lrp2*ΔPBD, 400 pg; *shroom3*, 200 pg; *eYFPvangl2*, 100 pg; and *LifeAct*, 400 pg. In all experiments, care was taken to exclude specimens that were not targeted correctly, i.e. in which fluorescence was not restricted to the neural plate or in which fluorescence could not be evaluated optimally at mid-neurula stages.

CRISPR/Cas9-mediated genome editing in Xenopus

Single guide RNAs (sgRNAs) were designed using CRISPRscan (CRISPRscan.org; Moreno-Mateos et al., 2015), synthesized from double-stranded template DNA using the MEGAscript T7 transcription kit (Invitrogen, AM1354) and purified using the MEGAclear transcription clean-up kit (Invitrogen, AM1908). Cas9 (PNA Bio, CP01-50) ribonucleic particles (CRNPs) were assembled by heating sgRNA to 70°C followed by immediate chilling to prevent formation of secondary structures and subsequent incubation with Cas9 at 37°C for 5 min. Per injection, a volume of 8 nl containing 1 ng Cas9/300 pg sgRNA was delivered into the animal pole of oocytes ~20 min after fertilization. To evaluate editing, DNA from a pool of ten embryos was harvested by lysis at the desired stage, PCR amplicons containing the cutting site were sequenced and knockout efficiency was calculated using the Synthego ICE online tool (ice.synthego.com; Hsiau et al., 2019 preprint).

Dextran uptake assay

Embryos at the 8-cell stage were injected unilaterally with *lrp2* MO and raised in 0.1×MBSH until stage 14, when the vitelline membrane was removed. Embryos were incubated in 0.1×MBSH containing 10 ng/μl dextran tetramethylrhodamine (Invitrogen, D1817) until stage 18. They were then transferred to fresh 0.1×MBSH and further reared until stage 20, fixed in PFA, washed, bisected at the level of the forebrain and further processed for staining and imaging.

Whole-mount *in situ* hybridization

Xenopus embryos were fixed for 2 h in 1×MEMFA at room temperature and further processed for *in situ* hybridization following standard protocols (Harland, 1991). The probe for *lrp2.L* was kindly provided by André Brändli (University Hospital and Ludwig-Maximilians-University Munich, Germany) (Christensen et al., 2008).

Immunofluorescence

Mouse

For standard whole-mount imaging, E8.5 mouse embryos were dissected and the rostral neural plate was collected. Tissue was fixed for 1 h in 4% PFA at room temperature, washed in 1×PBS and either dehydrated in a methanol series to be stored in 100% methanol at −20°C or directly subjected to the immunofluorescence (IF) protocol. Embryos were permeabilized with PBS-Triton X-100 (0.1%) for 15 min at room temperature and blocked with this solution containing 1% donkey serum and 2% BSA for 6 h at room temperature. Incubation with primary antibodies was carried out for 48 h at 4°C using the following dilutions: sheep anti-LRP2 antiserum (1:5000), kindly provided by the laboratory of Renata Kozyraki (Centre de Recherche des Cordeliers, INSERM, Université de Paris, France), rabbit anti-LRP2 (Abcam ab76969; 1:1000), mouse anti-ZO-1 (Invitrogen 33-9100; 1:100), mouse anti-ARL13b (UC Davis/NIH, NeuroMab 75-287; 1:500) and rabbit anti-GIPC1 (Alomone APZ-045; 1:200). Bound primary antibodies were visualized using secondary antibodies conjugated with Alexa Fluor 488, 555 and 647 after overnight incubation (Abcam ab150073, ab150106, ab150178 and ab150107; 1:500). All tissues were counterstained with DAPI (Invitrogen, 62248). Embryos were mounted with ProLong Gold Antifade Mountant (Invitrogen, P36934) in between two cover slips, using Secure-Seal Spacer (Invitrogen, S24737).

For IF on cryosections, PFA-fixed embryos were infiltrated with 15% and 30% sucrose in PBS up to 1 h, embedded in OCT (Tissue-Tek sa-4583) and cut into 10 μm coronal sections. Standard IF staining was carried out by incubation of tissue sections with primary antibodies overnight at 4°C at the following dilutions: mouse anti-acetylated tubulin (Sigma T7451; 1:1000), mouse anti-RAB11 (BD Transduction Laboratories 610657; 1:200), rabbit anti-VANGL2 (1:500; kindly provided by the laboratory of Mireille Montcouquiol, INSERM U1215, Bordeaux, France), sheep anti-LRP2 antiserum (1:5000; kindly provided by the laboratory of Renata Kozyraki), rabbit anti-NHERF1 (Alomone APZ-006; 1:500). Bound primary antibodies were visualized using secondary antibodies conjugated with Alexa Fluor 488, 555 and 647 after 1 h incubation at room temperature (Abcam ab150073, ab150106, ab150107 and ab150131; 1:500). All tissues were counterstained with DAPI (Invitrogen 62248). Sections were mounted with Dako fluorescence mounting medium (Agilent S302380-2).

For whole-mount STED imaging, E9.5 mouse embryos were collected and the neural tube was slit open using insect needles along the dorsal midline from caudal to rostral. The neural folds were precisely cut above the heart and placed on a sterile filter (Millipore MCEP06H48) with a drop of PBS (1×) in a Petri dish. The floor plate at the level of the cephalic flexure was pinched in order to unfold the tissue with the ventricular part facing up. Filters were placed in a six-well plate containing DMEM/10% FCS and explants were incubated at 37°C, with 5% CO₂ and 95% humidity for 3–4 h to flatten and recover. The explants were washed gently in 1×PBS, fixed for 1 h in 4% PFA and subjected to the standard IF protocol described above. Highly cross-absorbed secondary antibodies Alexa Fluor Plus 594 (Invitrogen A32744) and Atto 647N (Active Motif 15038) were used. Explants were flat-mounted in ProLong Gold Antifade Mountant (Invitrogen P36934) to obtain optimal resolution.

Xenopus

Embryos were fixed in a solution of 4% PFA in 1×PBS for 1 h at room temperature or overnight at 4°C, then washed in 1×PBS to remove fixative. For whole-mount staining, the vitelline membrane was carefully removed and embryos were transferred to CAS-blocking reagent (Invitrogen 008120). For staining of sections, embryos were fixed in 1×MEMFA, embedded in 2% agarose and sectioned on a Vibratome series 1000. The following primary antibodies were used at concentrations of 2–5 μg/ml: rabbit anti-Lrp2 (Abcam ab76969), mouse anti-MYC (clone 9E10, Abcam ab32), monoclonal mouse anti-α-Tubulin (clone DM1A, Sigma T6199), goat anti-Gipc1 (Sigma SAB2500463) and chicken anti-GFP (Invitrogen A10262). Where possible, subtype-specific secondary antibodies coupled to either AlexaFluor 488 or 555 were used (Invitrogen; 1:1000). AlexaFluor 405, 488 or 555-coupled phalloidin (Invitrogen A30104, A12379 or A34055, respectively; 1:100–1:200) was used to stain filamentous actin. DNA was stained with Hoechst 33342 (Invitrogen) to visualize nuclei.

Microscopy

Confocal microscopy, image processing and analysis

Image acquisitions of mouse tissue sections and mouse neural folds were carried out using a Leica SP8 confocal microscope with either HC PI Apo CS2 63× NA 1.4 oil immersion objective for sections or HC PI Apo 20× NA 0.75 MultiIMM with glycerol immersion for whole-mount imaging. The raw data from whole-mount mouse embryos were acquired close to the Nyquist sampling limit with a z-piezo stepper (80 nm pixel size, 0.5 μm z-step size 12 bit, dynamic range). In all samples, Alexa Fluor 488 was excited by a 488 nm laser, detection at 500–550 nm; Alexa Fluor 555 was excited by a 555 nm laser, detection at 570–620 nm; Alexa Fluor 647 was excited by a 633 nm or 647 nm laser, detection at 660–730 nm; and DAPI was excited at 405 nm, detection at 420–450 nm with a pinhole set to 1 AU. All samples that were compared either for qualitative or quantitative analysis were imaged under identical settings for laser power, detector and pixel size.

Confocal z-stacks of whole-mount neural folds were subjected to a background correction and processed by deconvolution with the CMLE algorithm and theoretical PSF in order to obtain an improved signal-to-noise ratio and axial and spatial resolution using Huygens Professional software (Scientific Volume Imaging). The deconvolution was applied to all image sets prior further segmentation and analysis steps with the Imaris Software. *Xenopus* samples were imaged on a Zeiss LSM5 Pascal or LSM700 confocal microscope.

STED imaging

En face STED images of mouse cephalic explants were taken with a Leica SP8 TCS STED microscope (Leica Microsystems) equipped with a pulsed white-light excitation laser (WLL; ~80 ps pulse width, 80 MHz repetition rate; NKT Photonics) and two STED lasers for depletion at 592 nm and 775 nm. The system was controlled by the Leica LAS X software. Dual-color STED imaging was performed by sequential excitation of Alexa Fluor Plus 594 at 590 nm and Atto 647N at 647 nm. For emission depletion, the 775 nm STED laser was used. Time-gated detection was set from 0.3 to 6 ns. Two hybrid detectors (HyD) were used at appropriate spectral regions separated from the STED laser to detect the fluorescence signals. The emission filter was set to 600–640 nm for Alexa Fluor Plus 594 and to 657–750 nm for Atto 647N. Images were sequentially acquired with a HC PL APO CS2 100×/1.40 NA oil immersion objective (Leica Microsystems), and a scanning format of 1024×1024 pixels, 8-bit sampling, 16× line averaging and 6× optical zoom, yielding a voxel dimension of 18.9×18.9 nm. In addition to every STED image, a confocal image with the same settings but only 1× line averaging was acquired.

Scanning electron microscopy

E8.5 embryos were dissected and fixed in 0.1 M sodium cacodylate buffer (pH 7.3/7.4) containing 2.5% glutaraldehyde. Rinsing in cacodylate buffer was followed by a postfixation step in 2% OsO₄ for 2 h. Samples were dehydrated in a graded ethanol series, osmicated, dried in critical point apparatus (Polaron 3000), coated with gold/palladium MED 020 (BAL-TEC) and examined using a Zeiss scanning electron microscope Gemini DSM 982.

Transmission electron microscopy

After dissection, mouse embryos at E9.5 were fixed with 3% formaldehyde in 0.2 M HEPES buffer (pH 7.4), for 30 min at room temperature followed by postfixation with 6% formaldehyde/0.1% glutaraldehyde in 0.2 M HEPES buffer for 24 h at 4°C. Samples were stained with 1% OsO₄ for 2 h, dehydrated in a graded ethanol series and propylene oxide, and embedded in Poly/Bed 812 (Polysciences). Ultrathin sections were contrasted with uranyl acetate and lead citrate. Sections were examined with a Thermo Fisher Morgagni electron microscope, digital images were captured with a Morada CCD camera and the iTEM software (EMSIS). The same software was used to manually measure the size of the average cell diameter.

Video-documentation of neural development

For videography of actin dynamics, *LifeAct* mRNA was injected into both dorsal blastomeres of albino embryos at the four-cell stage, followed by unilateral injection of *lrp2* MO at the eight-cell stage. Correct targeting was verified at early neural plate stages and only embryos targeted correctly into the neural lineage were used. A time series of single plane confocal images (pinhole >1 Airy unit to increase optical section thickness, one frame per minute) was recorded on a Zeiss LSM 700 using a 20× objective.

For bright-field imaging of neurulation, timelapse sequences of embryos injected unilaterally with *lrp2* MO were recorded at two frames per minute from stage 13 onwards on a Zeiss stereomicroscope (SteREO Discovery.V12) with an AxioCam HRc (Zeiss).

Measurements and statistics

Neural plate width quantification

For neural plate width measurement, control and treated embryos were photographed frontally after *in situ* hybridization for the pan-neural marker *sox3* and analyzed in ImageJ. The floor plate, easily identified by the lightest staining along the rostrocaudal neural midline, was marked and the widest part of the anterior neural plate was measured orthogonally to the midline. For each embryo, the ratio between injected and uninjected side was calculated.

Cell surface area quantification

The anterior neural folds of matching somite stage wild-type and mutant mouse embryos were subjected to cell surface area analysis. Regions of interest of the same size were chosen (four per sample) and cropped in 3D in IMARIS (Bitplane) from the whole-mount images. Using a maximum intensity projection in Fiji, they were transformed into 2D datasets. The Imaris Cell segmentation module was used for analysis, excluding incomplete cells from the edges. Manual adjustment was performed if necessary and final cell surface area parameters were extracted. The complete dataset was subjected to statistical analysis using an unpaired *t*-test.

In *Xenopus*, cell surface areas were measured manually using ImageJ. To that end, at least 30 cells from corresponding areas of uninjected and injected side of each embryo (i.e. 60 cells per embryo) were analyzed. The mean surface area of each side was calculated and used to determine a ratio between injected and uninjected side.

Statistical analysis

Where data are shown in box plots, the median is represented by the bold bar, the box represents the interquartile range, upper and lower whiskers extend 1.5 times the interquartile range, and outliers are shown as open circles. Statistical tests used to analyze the data were done using Prism 7 software (GraphPad) or Statistical R and are mentioned in the respective figure legends. Significance was scored as follows: $P \geq 0.05$, not significant; $P < 0.05$; * $P < 0.01$; ** $P < 0.001$; *** P -value levels. Numbers of specimens and biological replicates are reported in the figures or figure legends.

Acknowledgements

We thank Nora Mecklenburg for her intellectual input to the project. The professional assistance of Anje Sporbert and Matthias Richter with confocal microscopy, of Mrs Schrade, Bettina Purfürst and Christina Schiel with electron microscopy, and of Martin Lehmann and Hannes Gonschior with STED microscopy is gratefully acknowledged. Many thanks to Mireille Montcouquiol for kindly providing the VANGL2 antibody. We appreciate Manfred Ströhm's mouse husbandry work and Anke Scheer's technical assistance. We thank Gary Lewin for critical reading of

the manuscript and Thomas Willnow for acquisition of financial support for the project. Many thanks to Martin Blum and members of the zoology department for support and discussion, to Tim Ott for advice on CRISPR analysis, to Janes Odar for a macro to adjust z-projections, and to Ann-Kathrin Burkhart and Niklas Schaedler for their work on *Lrp2* during the initial steps of this project.

Competing interests

The authors declare no competing or financial interests.

Author contributions

Conceptualization: I.K., C.L., J.B.W., A.H., K.F.; Formal analysis: I.K.; Investigation: I.K., C.L., E.S., J.H., V.T., L.R., J.G., K.F.; Writing - original draft: I.K., A.H., K.F.; Writing - review & editing: I.K., C.L., J.B.W., A.H., K.F.; Visualization: I.K., C.L., K.F.; Supervision: J.B.W., A.H., K.F.; Project administration: J.B.W., A.H., K.F.; Funding acquisition: J.B.W., A.H., K.F.

Funding

A.H. was supported by the Deutsche Forschungsgemeinschaft, Collaborative Research Center (CRC958). I.K. was supported by the Deutsche Forschungsgemeinschaft Research Training Group grant (GRK2318, TJ-Train). K.F. was supported through a Margerete-von-Wrangell-Habilitationsstipendium, funded by the European Social Fund and by the Ministry of Science, Research and the Arts in Baden-Württemberg. C.L. and J.B.W. were supported by the Eunice Kennedy Shriver National Institute of Child Health and Human Development (R01HD099191) and the National Institute of General Medical Sciences (R01GM104853). Deposited in PMC for release after 12 months.

Supplementary information

Supplementary information available online at <https://dev.biologists.org/lookup/doi/10.1242/dev.195008.supplemental>

Peer review history

The peer review history is available online at <https://dev.biologists.org/lookup/doi/10.1242/dev.195008.reviewer-comments.pdf>

References

- Aschenbrenner, L., Lee, T. and Hasson, T. (2003). Myo6 facilitates the translocation of endocytic vesicles from cell peripheries. *Mol. Biol. Cell* **14**, 2728-2743. doi:10.1091/mbc.e02-11-0767
- Baardman, M. E., Zwier, M. V., Wisse, L. J., Gittenberger-de Groot, A. C., Kerstjens-Frederikse, W. S., Hofstra, R. M. W., Jurdzinski, A., Hierck, B. P., Jongbloed, M. R. M., Berger, R. M. F. et al. (2016). Common arterial trunk and ventricular non-compaction in *Lrp2* knockout mice indicate a crucial role of LRP2 in cardiac development. *Dis. Model. Mech.* **9**, 413-425. doi:10.1242/dmm.022053
- Balashova, O. A., Visina, O. and Borodinsky, L. N. (2017). Folate receptor 1 is necessary for neural plate cell apical constriction during *Xenopus* neural tube formation. *Development* **144**, 1518-1530. doi:10.1242/dev.137315
- Benmerah, A. (2013). The ciliary pocket. *Curr. Opin. Cell Biol.* **25**, 78-84. doi:10.1016/j.cob.2012.10.011
- Bertet, C., Sulak, L. and Lecuit, T. (2004). Myosin-dependent junction remodelling controls planar cell intercalation and axis elongation. *Nature* **429**, 667-671. doi:10.1038/nature02590
- Butler, M. T., Wallingford, J. B., (2018). Spatial and temporal analysis of PCP protein dynamics during neural tube closure. *eLife* **7**, 773. <http://doi.org/10.7554/eLife.36456>
- Cases, O., Joseph, A., Obry, A., Santin, M. D., Ben-Yacoub, S., Pâques, M., Amsellem-Levera, S., Bribian, A., Simonutti, M., Augustin, S. et al. (2015). Foxg1-Cre mediated *Lrp2* inactivation in the developing mouse neural retina, ciliary and retinal pigment epithelia models congenital high myopia. *PLoS ONE* **10**, e0129518. doi:10.1371/journal.pone.0129518
- Chen, W. J., Goldstein, J. L. and Brown, M. S. (1990). NPXY, a sequence often found in cytoplasmic tails, is required for coated pit-mediated internalization of the low density lipoprotein receptor. *J. Biol. Chem.* **265**, 3116-3123.
- Christ, A., Christa, A., Kur, E., Lioubinski, O., Bachmann, S., Willnow, T. E. and Hammes, A. (2012). LRP2 is an auxiliary SHH receptor required to condition the forebrain ventral midline for inductive signals. *Dev. Cell* **22**, 268-278. doi:10.1016/j.devcel.2011.11.023
- Christ, A., Marczenke, M. and Willnow, T. E. (2020). LRP2 controls sonic hedgehog-dependent differentiation of cardiac progenitor cells during outflow tract formation. *Hum. Mol. Genet.* **29**, 3183-3196. doi:10.1093/hmg/ddaa200
- Christensen, E. I., Raciti, D., Reggiani, L., Verroust, P. J. and Brändli, A. W. (2008). Gene expression analysis defines the proximal tubule as the compartment for endocytic receptor-mediated uptake in the *Xenopus* pronephric kidney. *Pflugers Arch.* **456**, 1163-1176. doi:10.1007/s00424-008-0488-3
- Christodoulou, N. and Skourides, P. A. (2015). Cell-autonomous Ca²⁺ flashes elicit pulsed contractions of an apical actin network to drive apical constriction

- during neural tube closure. *Cell Rep* **13**, 2189-2202. doi:10.1016/j.celrep.2015.11.017
- Colas, J. F. and Schoenwolf, G. C.** (2001). Towards a cellular and molecular understanding of neurulation. *Dev. Dyn.* **221**, 117-145. doi:10.1002/dvdy.1144
- Copp, A. J., Greene, N. D. E. and Murdoch, J. N.** (2003). Dishevelled: linking convergent extension with neural tube closure. *Trends Neurosci.* **26**, 453-455. doi:10.1016/S0166-2236(03)00212-1
- Darken, R. S., Scola, A. M., Rakeman, A. S., Das, G., Mlodzik, M. and Wilson, P. A.** (2002). The planar polarity gene *strabismus* regulates convergent extension movements in *Xenopus*. *EMBO J.* **21**, 976-985. doi:10.1093/emboj/21.5.976
- Eaton, S. and Martin-Belmonte, F.** (2014). Cargo sorting in the endocytic pathway: a key regulator of cell polarity and tissue dynamics. *Cold Spring Harb. Perspect Biol.* **6**, a016899-a016899. doi:10.1101/cshperspect.a016899
- Fabrowski, P., Necakov, A. S., Mumbauer, S., Loeser, E., Reversi, A., Streichan, S., Briggs, J. A. G. and De Renzi, S.** (2013). Tubular endocytosis drives remodelling of the apical surface during epithelial morphogenesis in *Drosophila*. *Nat. Commun.* **4**, 2244. doi:10.1038/ncomms3244
- Gauthier, N. C., Masters, T. A. and Sheetz, M. P.** (2012). Mechanical feedback between membrane tension and dynamics. *Trends Cell Biol.* **22**, 527-535. doi:10.1016/j.tcb.2012.07.005
- Giese, A. P., Ezan, J., Wang, L., Lasvaux, L., Lembo, F., Mazzocco, C., Richard, E., Reboul, J., Borg, J.-P., Kelley, M. W. et al.** (2012). *Gipc1* has a dual role in Vangl2 trafficking and hair bundle integrity in the inner ear. *Development* **139**, 3775-3785. doi:10.1242/dev.074229
- Giroto, G., Morgan, A., Krishnamoorthy, N., Cocca, M., Brumat, M., Bassani, S., La Bianca, M., Di Stazio, M. and Gasparini, P.** (2019). Next generation sequencing and animal models reveal SLC9A3R1 as a new gene involved in human age-related hearing loss. *Front. Genet.* **10**, 142. doi:10.3389/fgene.2019.00142
- Goto, T. and Keller, R.** (2002). The planar cell polarity gene *strabismus* regulates convergence and extension and neural fold closure in *Xenopus*. *Dev. Biol.* **247**, 165-181. doi:10.1006/dbio.2002.0673
- Gotthardt, M., Trommsdorff, M., Nevitt, M. F., Shelton, J., Richardson, J. A., Stockinger, W., Nimpf, J. and Herz, J.** (2000). Interactions of the low density lipoprotein receptor gene family with cytosolic adaptor and scaffold proteins suggest diverse biological functions in cellular communication and signal transduction. *J. Biol. Chem.* **275**, 25616-25624. doi:10.1074/jbc.M000955200
- Greene, N. D. E. and Copp, A. J.** (2014). Neural tube defects. *Annu. Rev. Neurosci.* **37**, 221-242. doi:10.1146/annurev-neuro-062012-170354
- Haigo, S. L., Hildebrand, J. D., Harland, R. M. and Wallingford, J. B.** (2003). Shroom induces apical constriction and is required for hinge-point formation during neural tube closure. *CURBIO* **13**, 2125-2137. doi:10.1016/j.cub.2003.11.054
- Hammes, A., Andreassen, T. K., Spoelgen, R., Raila, J., Hubner, N., Schulz, H., Metzger, J., Schweigert, F. J., Lippa, P. B., Nykjaer, A. et al.** (2005). Role of endocytosis in cellular uptake of sex steroids. *Cell* **122**, 751-762. doi:10.1016/j.cell.2005.06.032
- Harland, R. M.** (1991). In situ hybridization: an improved whole-mount method for *Xenopus* embryos. *Methods Cell Biol.* **36**, 685-695. doi:10.1016/S0091-679X(08)60307-6
- Hildebrand, J. D. and Soriano, P.** (1999). Shroom, a PDZ domain-containing actin-binding protein, is required for neural tube morphogenesis in mice. *Cell* **99**, 485-497. doi:10.1016/S0092-8674(00)81537-8
- Hsiao, T., Conant, D., Rossi, N., Maures, T., Waite, K., Yang, J., Joshi, S., Kelso, R., Holden, K., Enzmann, B. L. et al.** (2019). Inference of CRISPR edits from sanger trace data. *bioRxiv* 251082. doi:10.1101/251082
- Kantarci, S., Al-Gazali, L., Hill, R. S., Donnai, D., Black, G. C. M., Bieth, E., Chassaing, N., Lacombe, D., Devriendt, K., Teebi, A. et al.** (2007). Mutations in LRP2, which encodes the multiligand receptor megalin, cause Donnai-Barrow and facio-oculo-acoustico-renal syndromes. *Nat. Genet.* **39**, 957-959. doi:10.1038/ng2063
- Khalilii, H., Sull, A., Sarin, S., Boivin, F. J., Halabi, R., Svajger, B., Li, A., Cui, V. W., Drysdale, T. and Bridgewater, D.** (2016). Developmental origins for kidney disease due to shroom3 deficiency. *J. Am. Soc. Nephrol.* **27**, 2965-2973. doi:10.1681/ASN.2015060621
- Kur, E., Mecklenburg, N., Cabrera, R. M., Willnow, T. E. and Hammes, A.** (2014). LRP2 mediates folate uptake in the developing neural tube. *J. Cell Sci.* **127**, 2261-2268. doi:10.1242/jcs.140145
- Kurth, T. and Hausen, P.** (2000). Bottle cell formation in relation to mesodermal patterning in the *Xenopus* embryo. *Mech. Dev.* **97**, 117-131. doi:10.1016/S0925-4773(00)00428-7
- Lee, J.-Y. and Harland, R. M.** (2010). Endocytosis is required for efficient apical constriction during *Xenopus* gastrulation. *Curr. Biol.* **20**, 253-258. doi:10.1016/j.cub.2009.12.021
- Lee, C., Scherr, H. M. and Wallingford, J. B.** (2007). Shroom family proteins regulate g-tubulin distribution and microtubule architecture during epithelial cell shape change. *Development* **134**, 1431-1441. doi:10.1242/dev.02828
- Löfberg, J.** (1974). Apical surface topography of invaginating and noninvaginating cells. A scanning-transmission study of amphibian neurulae. *Dev. Biol.* **36**, 311-329. doi:10.1016/0012-1606(74)90054-2
- Martin, A. C. and Goldstein, B.** (2014). Apical constriction: themes and variations on a cellular mechanism driving morphogenesis. *Development* **141**, 1987-1998. doi:10.1242/dev.102228
- Martin, A. C., Kaschube, M. and Wieschaus, E. F.** (2009). Pulsed contractions of an actin-myosin network drive apical constriction. *Nature* **457**, 495-499. doi:10.1038/nature07522
- Martin, J. B., Muccioli, M., Herman, K., Finnell, R. H. and Plageman, T. F.** (2019). Folic acid modifies the shape of epithelial cells during morphogenesis via a Fcrl1 and MLCK dependent mechanism. *Biol. Open* **8**, bio041160. doi:10.1242/bio.041160
- McGreevy, E. M., Vijayraghavan, D., Davidson, L. A. and Hildebrand, J. D.** (2015). Shroom3 functions downstream of planar cell polarity to regulate myosin II distribution and cellular organization during neural tube closure. *Biol. Open* **4**, 186-196. doi:10.1242/bio.20149589
- Miao, H., Vanderleest, T. E., Jewett, C. E., Loerke, D. and Blankenship, J. T.** (2019). Cell ratcheting through the Sbf RabGEF directs force balancing and stepped apical constriction. *J. Cell Biol.* **218**, 3845-3860. doi:10.1083/jcb.201905082
- Molla-Herman, A., Ghossoub, R., Blisnick, T., Meunier, A., Serres, C., Silbermann, F., Emmerson, C., Romeo, K., Bourdoncle, P., Schmitt, A. et al.** (2010). The ciliary pocket: an endocytic membrane domain at the base of primary and motile cilia. *J. Cell Sci.* **123**, 1785-1795. doi:10.1242/jcs.059519
- Moreno-Mateos, M. A., Vejnar, C. E., Beaudoin, J.-D., Fernández, J. P., Mis, E. K., Khokha, M. K. and Giraldez, A. J.** (2015). CRISPRscan: designing highly efficient sgRNAs for CRISPR-Cas9 targeting in vivo. *Nat. Methods* **12**, 982-988. doi:10.1038/nmeth.3543
- Naccache, S. N., Hasson, T. and Horowitz, A.** (2006). Binding of internalized receptors to the PDZ domain of GIPC/synectin recruits myosin VI to endocytic vesicles. *Proc. Natl. Acad. Sci. USA* **103**, 12735-12740. doi:10.1073/pnas.0605317103
- Nikolopoulou, E., Galea, G. L., Rolo, A., Greene, N. D. E. and Copp, A. J.** (2017). Neural tube closure: cellular, molecular and biomechanical mechanisms. *Development* **144**, 552-566. doi:10.1242/dev.145904
- Nishimura, T., Honda, H. and Takeichi, M.** (2012). Planar cell polarity links axes of spatial dynamics in neural-tube closure. *Cell* **149**, 1084-1097. doi:10.1016/j.cell.2012.04.021
- Nykjaer, A. and Willnow, T. E.** (2002). The low-density lipoprotein receptor gene family: a cellular Swiss army knife? *Trends Cell Biol.* **12**, 273-280. doi:10.1016/S0962-8924(02)02282-1
- Ossipova, O., Kim, K., Lake, B. B., Itoh, K., Ioannou, A. and Sokol, S. Y.** (2014). Role of Rab11 in planar cell polarity and apical constriction during vertebrate neural tube closure. *Nat. Commun.* **5**, 3734. doi:10.1038/ncomms4734
- Ossipova, O., Chuykin, I., Chu, C.-W. and Sokol, S. Y.** (2015a). Vangl2 cooperates with Rab11 and Myosin V to regulate apical constriction during vertebrate gastrulation. *Development* **42**, 99-107. doi:10.1242/dev.111161
- Ossipova, O., Kim, K. and Sokol, S. Y.** (2015b). Planar polarization of Vangl2 in the vertebrate neural plate is controlled by Wnt and Myosin II signaling. *Biol. Open* **4**, 722-730. doi:10.1242/bio.201511676
- Ozdemir, H., Plamondon, J., Gaskin, P., Asoglu, M. R. and Turan, S.** (2020). A prenatally diagnosed case of Donnai-Barrow syndrome: Highlighting the importance of whole exome sequencing in cases of consanguinity. *Am. J. Med. Genet. A* **182**, 289-292. doi:10.1002/ajmg.a.61428
- Pawson, C. T. and Scott, J. D.** (2010). Signal integration through blending, bolstering and bifurcating of intracellular information. *Nat. Struct. Mol. Biol.* **17**, 653-658. doi:10.1038/nsmb.1843
- Peshkin, L., Lukyanov, A., Kalocsay, M., Gage, R. M., Wang, D., Pells, T. J., Karimi, K., Vize, P. D., Wühr, M. and Kirschner, M. W.** (2019). The protein repertoire in early vertebrate embryogenesis. *bioRxiv*, 571174. doi:10.1101/571174
- Rebekah Prasoona, K., Sunitha, T., Srinadh, B., Muni Kumari, T. and Jyothy, A.** (2018). LRP2 gene variants and their haplotypes strongly influence the risk of developing neural tube defects in the fetus: a family-triad study from South India. *Metab. Brain Dis.* **33**, 1343-1352. doi:10.1007/s11011-018-0242-2
- Reed, B. C., Cefalu, C., Bellaire, B. H., Cardelli, J. A., Louis, T., Salamon, J., Bloecher, M. A. and Bunn, R. C.** (2005). GLUT1CBP(TIP2/GIPC1) interactions with GLUT1 and myosin VI: evidence supporting an adapter function for GLUT1CBP. *Mol. Biol. Cell* **16**, 4183-4201. doi:10.1091/mbc.e04-11-0978
- Renard, E., Chéry, C., Oussalah, A., Josse, T., Perrin, P., Tramoy, D., Voirin, J., Klein, O., Leheup, B., Feillet, F. et al.** (2019). Exome sequencing of cases with neural tube defects identifies candidate genes involved in one-carbon/vitamin B12 metabolisms and Sonic Hedgehog pathway. *Hum. Genet.* **138**, 703-713. doi:10.1007/s00439-019-02015-7
- Rosenfeld, J. A., Ballif, B. C., Martin, D. M., Aylsworth, A. S., Bejjani, B. A., Torchia, B. S. and Shaffer, L. G.** (2010). Clinical characterization of individuals with deletions of genes in holoprosencephaly pathways by aCGH finds the phenotypic spectrum of HPE. *Hum. Genet.* **127**, 421-440. doi:10.1007/s00439-009-0778-7
- Roszkó, I., Sepich, D. S., Jessen, J. R., Chandrasekhar, A. and Solnica-Krezel, L.** (2015). A dynamic intracellular distribution of Vangl2 accompanies cell

- polarization during zebrafish gastrulation. *Development* **142**, 2508-2520. doi:10.1242/dev.119032
- Sabatino, J. A., Stokes, B. A. and Zohn, I. E.** (2017). Prevention of neural tube defects in Lrp2 mutant mouse embryos by folic acid supplementation. *Birth Defects Res.* **109**, 16-26. doi:10.1002/bdra.23589
- Saito, A., Pietromonaco, S., Loo, A. K. and Farquhar, M. G.** (1994). Complete cloning and sequencing of rat gp330/megalin, a distinctive member of the low density lipoprotein receptor gene family. *Proc. Natl. Acad. Sci. USA* **91**, 9725-9729. doi:10.1073/pnas.91.21.9725
- Schroeder, T. E.** (1970). Neurulation in *Xenopus laevis*. An analysis and model based upon light and electron microscopy. *J. Embryol. Exp. Morphol.* **23**, 427-462.
- Session, A. M., Uno, Y., Kwon, T., Chapman, J. A., Toyoda, A., Takahashi, S., Fukui, A., Hikosaka, A., Suzuki, A., Kondo, M. et al.** (2016). Genome evolution in the allotetraploid frog *Xenopus laevis*. *Nature* **538**, 336-343. doi:10.1038/nature19840
- Shenolikar, S., Voltz, J. W., Minkoff, C. M., Wade, J. B. and Weinman, E. J.** (2002). Targeted disruption of the mouse NHERF-1 gene promotes internalization of proximal tubule sodium-phosphate cotransporter type IIa and renal phosphate wasting. *Proc. Natl. Acad. Sci. USA* **99**, 11470-11475. doi:10.1073/pnas.162232699
- Slatery, C., Jenkin, K. A., Lee, A., Simcocks, A. C., McAinch, A. J., Poronnik, P. and Hryciw, D. H.** (2011). Na⁺-H⁺ exchanger regulatory factor 1 (NHERF1) PDZ scaffold binds an internal binding site in the scavenger receptor megalin. *Cell. Physiol. Biochem.* **27**, 171-178. doi:10.1159/000325219
- Spoelgen, R., Hammes, A., Anzenberger, U., Zechner, D., Andersen, O. M., Jerchow, B. and Willnow, T. E.** (2005). LRP2/megalin is required for patterning of the ventral telencephalon. *Development* **132**, 405-414. doi:10.1242/dev.01580
- Sutherland, A., Keller, R. and Lesko, A.** (2020). Convergent extension in mammalian morphogenesis. *Semin. Cell Dev. Biol.* **100**, 199-211. doi:10.1016/j.semcdb.2019.11.002
- Tan, C., Deardorff, M. A., Saint-Jeannet, J. P., Yang, J., Arzoumanian, A. and Klein, P. S.** (2001). Kermit, a frizzled interacting protein, regulates frizzled 3 signaling in neural crest development. *Development* **128**, 3665-3674.
- Wallingford, J. B.** (2005). Neural tube closure and neural tube defects: studies in animal models reveal known knowns and known unknowns. *Am. J. Med. Genet. C Semin. Med. Genet.* **135C**, 59-68. doi:10.1002/ajmg.c.30054
- Wallingford, J. B., Rowning, B. A., Vogeli, K. M., Rothbacher, U., Fraser, S. E. and Harland, R. M.** (2000). Dishevelled controls cell polarity during *Xenopus* gastrulation. *Nature* **405**, 81-85. doi:10.1038/35011077
- Wallingford, J. B., Niswander, L. A., Shaw, G. M. and Finnell, R. H.** (2013). The continuing challenge of understanding, preventing, and treating neural tube defects. *Science* **339**, 1222002-1222002. doi:10.1126/science.1222002
- Weinman, E. J., Steplock, D., Tate, K., Hall, R. A., Spurney, R. F. and Shenolikar, S.** (1998). Structure-function of recombinant Na/H exchanger regulatory factor (NHE-RF). *J. Clin. Invest.* **101**, 2199-2206. doi:10.1172/JCI204
- Wicher, G. and Aldskogius, H.** (2008). Megalin deficiency induces critical changes in mouse spinal cord development. *Neuroreport* **19**, 559-563. doi:10.1097/WNR.0b013e3282f94267
- Williams, M., Yen, W., Lu, X. and Sutherland, A.** (2014). Distinct apical and basolateral mechanisms drive planar cell polarity-dependent convergent extension of the mouse neural plate. *Dev. Cell* **29**, 34-46. doi:10.1016/j.devcel.2014.02.007
- Willnow, T. E., Hilpert, J., Armstrong, S. A., Rohlmann, A., Hammer, R. E., Burns, D. K. and Herz, J.** (1996). Defective forebrain development in mice lacking gp330/megalin. *Proc. Natl. Acad. Sci. USA* **93**, 8460-8464. doi:10.1073/pnas.93.16.8460
- Ybot-Gonzalez, P., Cogram, P., Gerrelli, D. and Copp, A. J.** (2002). Sonic hedgehog and the molecular regulation of mouse neural tube closure. *Development* **129**, 2507-2517.
- Yuseff, M. I., Farfán, P., Bu, G. and Marzolo, M.-P.** (2007). A cytoplasmic PPPSP motif determines megalin's phosphorylation and regulates receptor's recycling and surface expression. *Traffic* **8**, 1215-1230. doi:10.1111/j.1600-0854.2007.00601.x

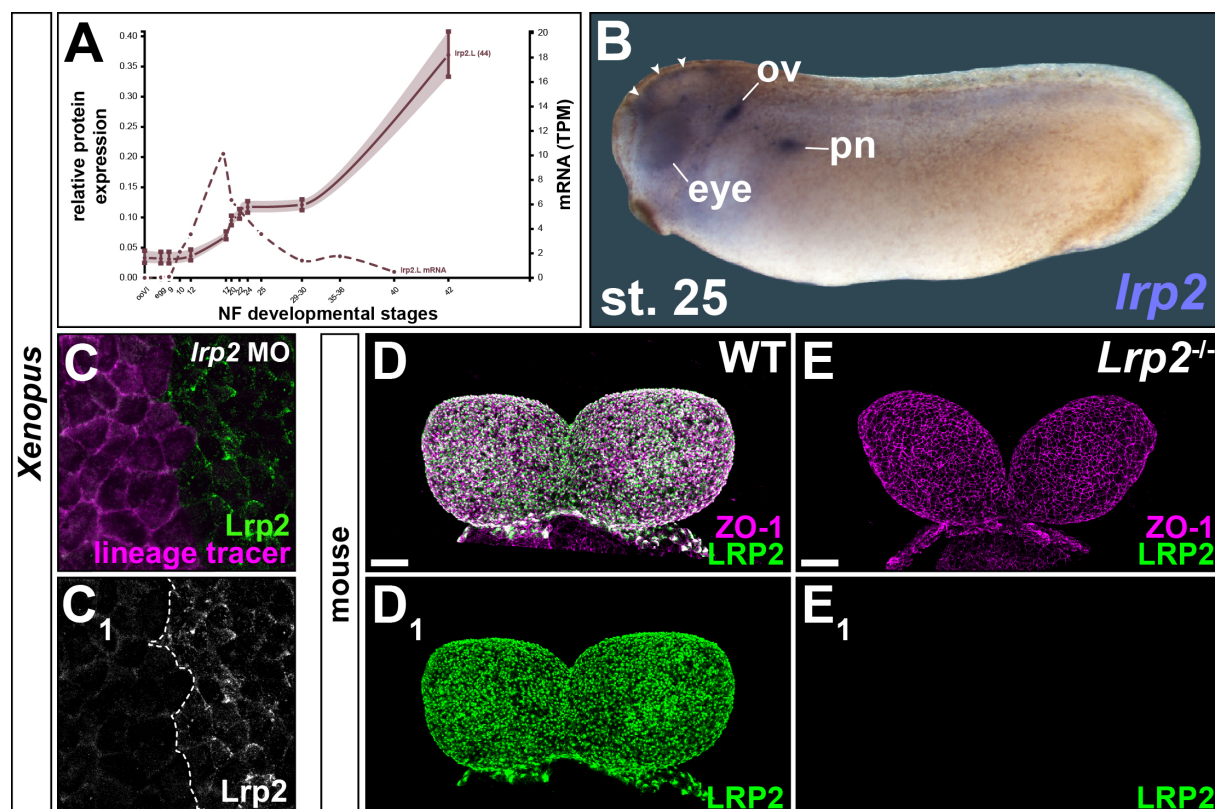


Fig. S1: Lrp2 expression and protein depletion by knock-down in *Xenopus* and knock-out in mouse. (A) mRNA and protein expression profile of *Xenopus lrp2.L* (from Xenbase.org). (B) *Xenopus lrp2* expressed in brain (arrowheads), eye anlage, otic vesicle (ov) and proximal pronephros (pn) in stage (st.) 25 tailbud embryo. (C) Morpholino oligomer (MO) decreases Lrp2 expression in injected cells; single channel (C₁) for clarity. (D, E) Frontal views of anterior neural folds of wild type (WT; D) and *Lrp2*^{-/-} (E) mouse embryos at embryonic day (E) 8.5. (D₁, E₁) WT LRP2 expression (D₁) lost in *Lrp2*^{-/-} (E₁). ZO-1 labels cell boundaries. Scale bars (D, E): 50 μm.

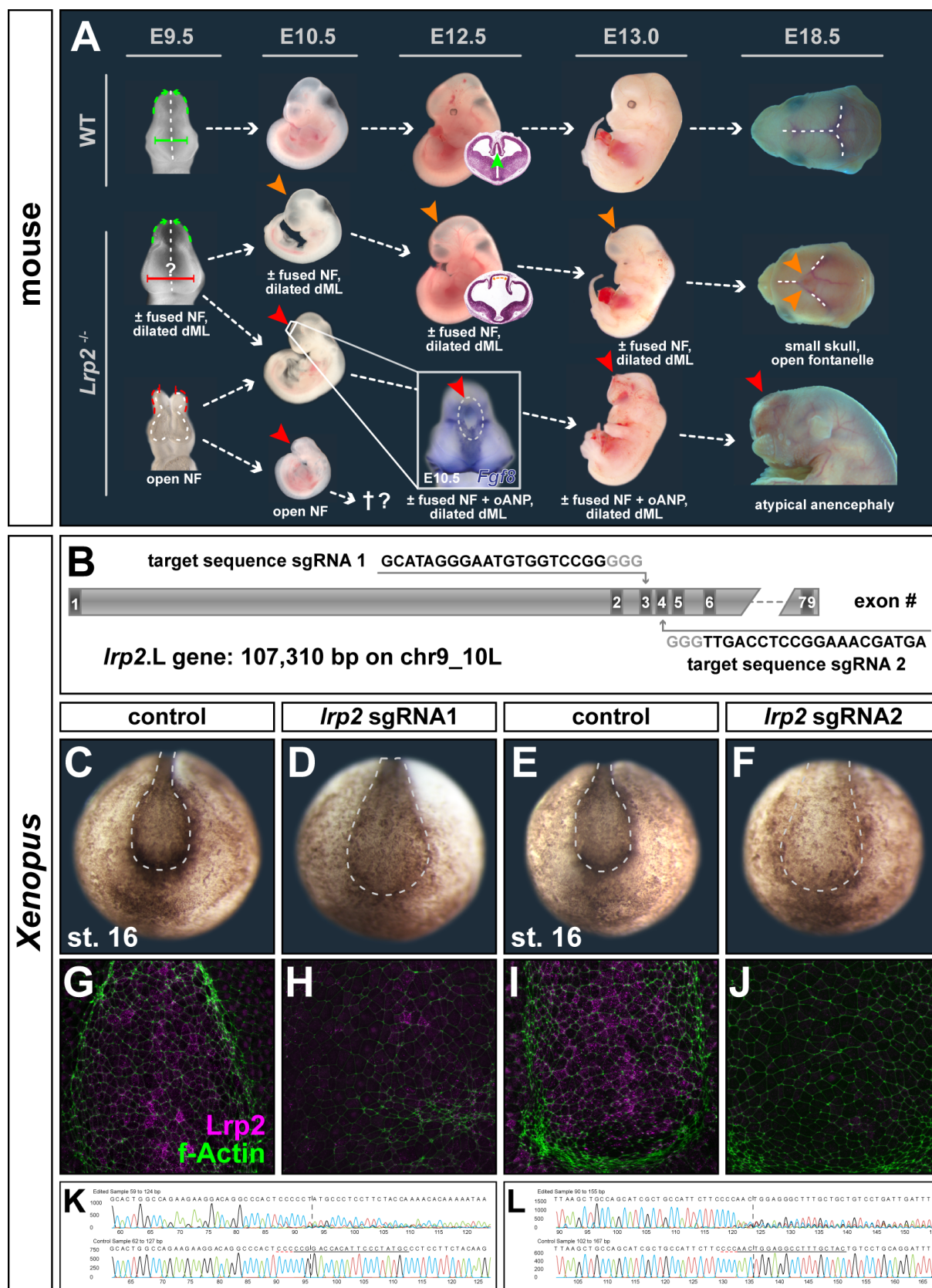


Fig. S2: Mouse neural tube closure phenotypes and CRISPR-Cas9-mediated genome editing of *Lrp2.L* in *Xenopus laevis*. (A) A putative developmental time line of neural tube (NT) defects (NTDs) in *Lrp2*^{-/-} mouse embryos. Note that embryos are not strictly to scale between stages, emphasis is on visualization of NTD progression. Top row: wild type (WT)

embryos at embryonic day (E) 9.5, 10.5, 12.5, 13.0 and 18.5. Lower rows: *Lrp2*^{-/-} embryos of the respective stage (st.). Frontal views of heads at E9.5 and inset in E10.5, lateral views of whole embryos at E10.5 through E13.0. E18.5: top views of heads in upper two specimens, lateral view of lower specimen. In all WT embryos from E9.5 onwards, the neural tube was closed (green arrows) and telencephalic neural folds (NF) were fused, creating a continuous dorsal midline (dML; white dotted line). The closed NT has a normal width (green bar). Two phenotypes of *Lrp2*^{-/-} embryos at E9.5: the NT was either closed with a dilated dML (red bar) or entirely open (red and white dotted lines). Question mark on the dML indicates a putatively open anterior neuropore (ANP), which was not readily visible at E9.5. From E10.5 onwards, three putative “lineages” of development could be tracked: **1)** orange markers - embryos with a more or less (\pm) closed NF and dilated dML (orange arrowheads), readily visible on transverse sections at E12.5 (compare area indicated by green arrowhead in WT and area indicated by orange line in mutant). These embryos most likely gave rise to embryos at E18.5 with a short head and open fontanelle, through which choroid plexus tissue can protrude (cf. Fig. 3A in (Willnow et al., 1996)). **2)** red markers - embryos with \pm fused NF that had a readily visible opening at the level of the ANP (red arrowheads), visualized via *Fgf8* expression in the dML at E10.5 (inset). In such embryos, the open (o) ANP probably increased in size (E13.0), leading to exposure and extrusion of NT tissue (cf. Fig. 2E, (Spoelgen et al., 2005)), finally causing atrophy of anteriormost brain tissue which culminated in an atypical form of anencephaly at E18.5. **3)** growth-retarded embryos at E10.5 had open neural folds and probably died after mid-gestation due to cardiovascular defects (Baardman et al., 2016; Christ et al., 2020). Numbers of *Lrp2*^{-/-} embryos at **E9.5 and E10.5** with fused NF and dilated dML (oANP not visible, therefore not scored): 33 / 51, 65 %; with open NF: 18 / 51, 35 %. Embryos at **E12.5 and E13.0** with fused NF and dilated dML with a range of closed to wide open ANP: 22 / 22 100 %; no embryos with open NF. Over the past five years, about 2 / 3 of embryos at **E18.5** with shortened skull and open fontanelle, 1 / 3 with atypical anencephaly. **(B)** Schematic representation of *Xenopus laevis* *lrp2*.L gene structure; target sequence for single guide (sg) RNA-binding in exon 3 and 4 is shown, protospacer-adjacent motif (PAM) in gray letters. **(C-J)** Injection of Cas9-ribonucleic particles (CRNP) assembled with sgRNA1 or 2 into zygotes impaired neural plate narrowing and lengthening **(C-F)** and reduced *Lrp2* **(G-J)** in CRISPRants compared to controls. f-Actin marks cell circumference. **(K, L)** Analysis of sequence flanking target sites confirmed editing in CRNP-injected samples (top row) compared to control samples (lower row).

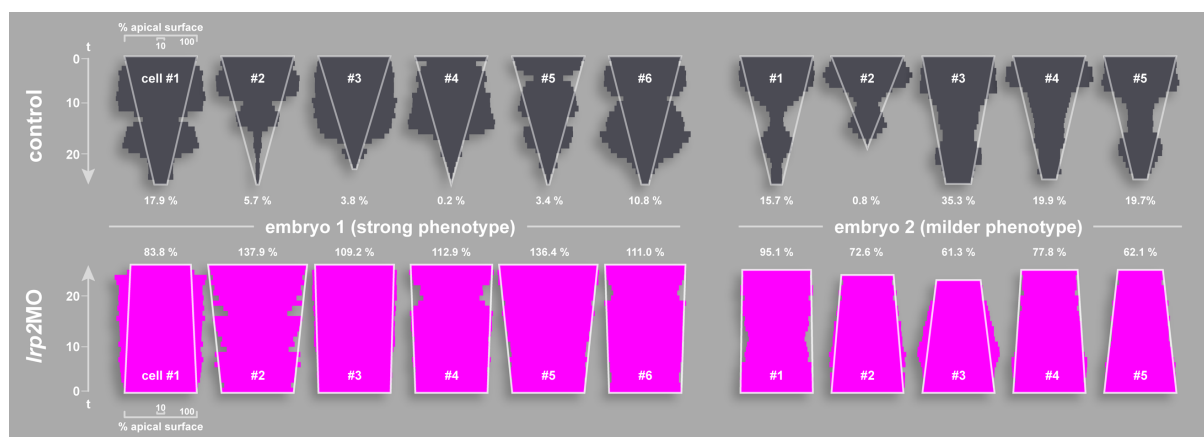


Fig. S3: Cell surface area fluctuation during apical constriction. Temporal development of the surface area of individual cells from two independent live-imaged embryos was plotted. Every horizontal bar represents the measurement at one time point (t) of a cell from either the uninjected control side (dark grey) or from the side injected with *Irp2MO* (identified by lineage tracer fluorescence; magenta). Wherever possible, up to 25 time points representing 120 min of live imaging were measured. For each cell, the cell surface size at t_0 was set to 100 % and the relative cell size at the end of the time series is shown. Note that the change in surface area is not continuous and linear (linear development indicated by white rectangles / triangles), but that surface area decreases and increases multiple times before finalizing apical constriction. These fluctuations are pronounced in control cells, but also present in *Irp2MO*-injected cells.

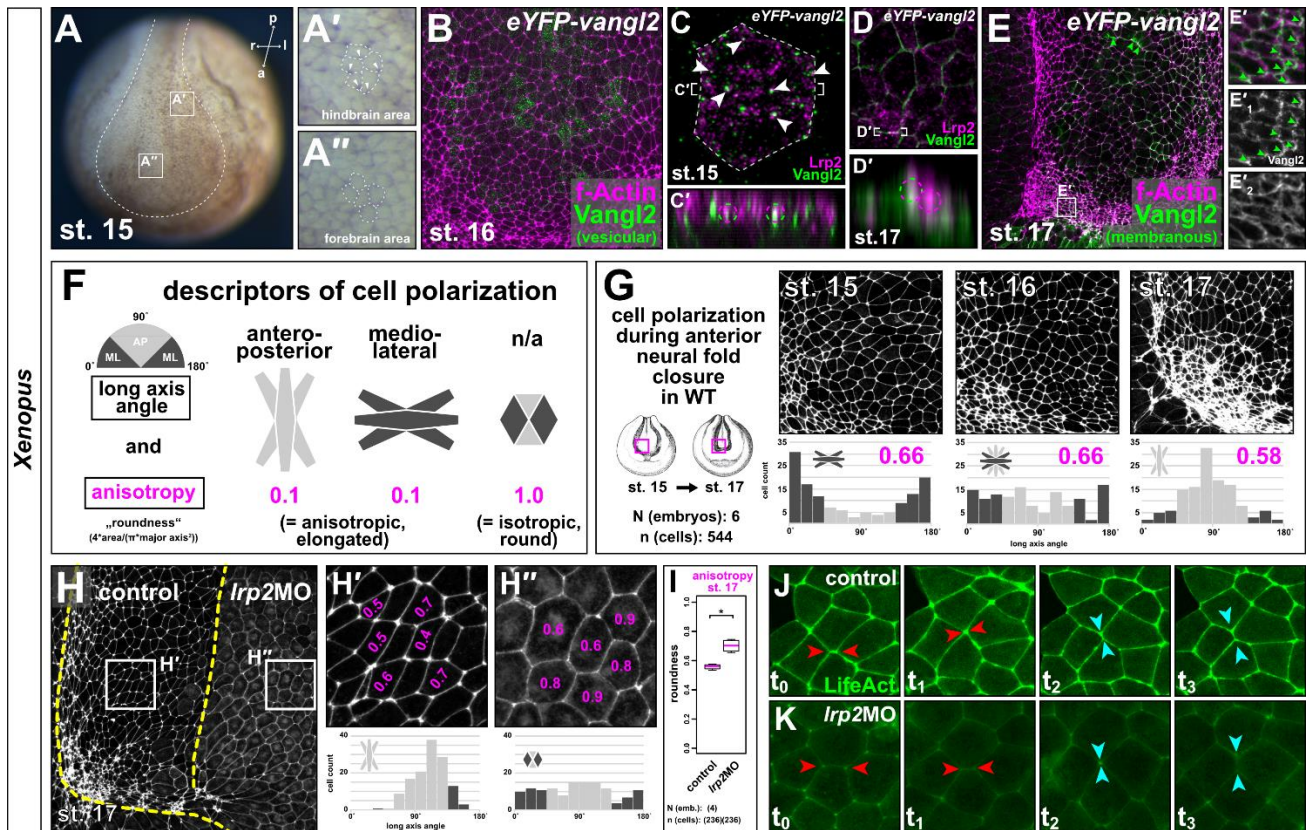


Fig. S: Dynamic planar cell polarity in the *Xenopus* neural plate. (A) Brightfield image; frontal view of a stage (st.) 15 embryo, note asymmetric pigment accumulation in anterior (a) aspect of cells (outlined by dashed line) in the hindbrain area (arrowheads in A') compared to symmetric circumferential distribution in forebrain area cells (A''). (B-D) *eYFP-vangl2* was injected into A1-lineage in 4-8-cell embryos and detected using indirect immunofluorescence (IF) for GFP, f-Actin visualizes cell borders. *eYFP-Vangl2* localized in dotted, vesicle-like pattern up to st. 16 (B; 6 embryos, st. 14-16). (C) Single forebrain area cell at st. 15, IF demonstrating overlap of *Vangl2* and *Lrp2* in several spots throughout the cell. (C') Optical section, level indicated in (C), colored circles indicate overlap. (D) Group of forebrain area cells at st. 17; *Vangl2* at membrane, *Lrp2* mostly cytoplasmic. (D') Optical section, level indicated in (D), colored circles indicate (non-)overlap. (E) Re-distribution to (asymmetric) membrane localization from st. 17 onwards (arrowheads in E and E' indicate *Vangl2* asymmetry; 8 embryos, st. 17 / 18). Magnified area (E') as indicated in (E); (E'_{1,2}) single channels shown in grayscale. (F) Schematic, describing two aspects of cell polarization - orientation of the long axis of a polarized cell and cell anisotropy. The long axis of a cell can be oriented in anteroposterior (AP; angles 45.1-135°, light grey) or mediolateral (ML; angles 0-45 and 135.1-180°, dark grey) direction. Cells featuring a long axis are anisotropic, with a "roundness" of 0.1 representing a narrow, elongated cell. At 1.0, cells are isotropic and consequentially do not feature a long axis. (G) Assessment of cell polarization during anterior neural fold narrowing in wildtype (WT) embryos from st. 15 to 17. Throughout this time window, cells are anisotropic (magenta numbers), but shift their planar orientation from ML (st. 15) via random (st. 16) to AP (st. 17). (H) Unilateral injection of *lrp2MO* into the A1-lineage of 8-cell embryos, cell polarity analysis at st. 17. Note anisotropic, AP-oriented cells in control (H') and more isotropic cells with randomly oriented long axes upon loss of *lrp2* (H''). (I) Graphical representation of reduced anisotropy upon loss of *lrp2*; Wilcoxon rank sum test, * = ≤ 0.05 . (J, K) Stills from

movies of embryos injected with LifeAct at 4-8-cells, T1-transitions between two pairs of cells are visualized over four time points (t). Red arrowheads: shortening cell junction in ML orientation; blue arrowheads: lengthening cell junction in AP orientation. l: left, p: posterior, r: right.

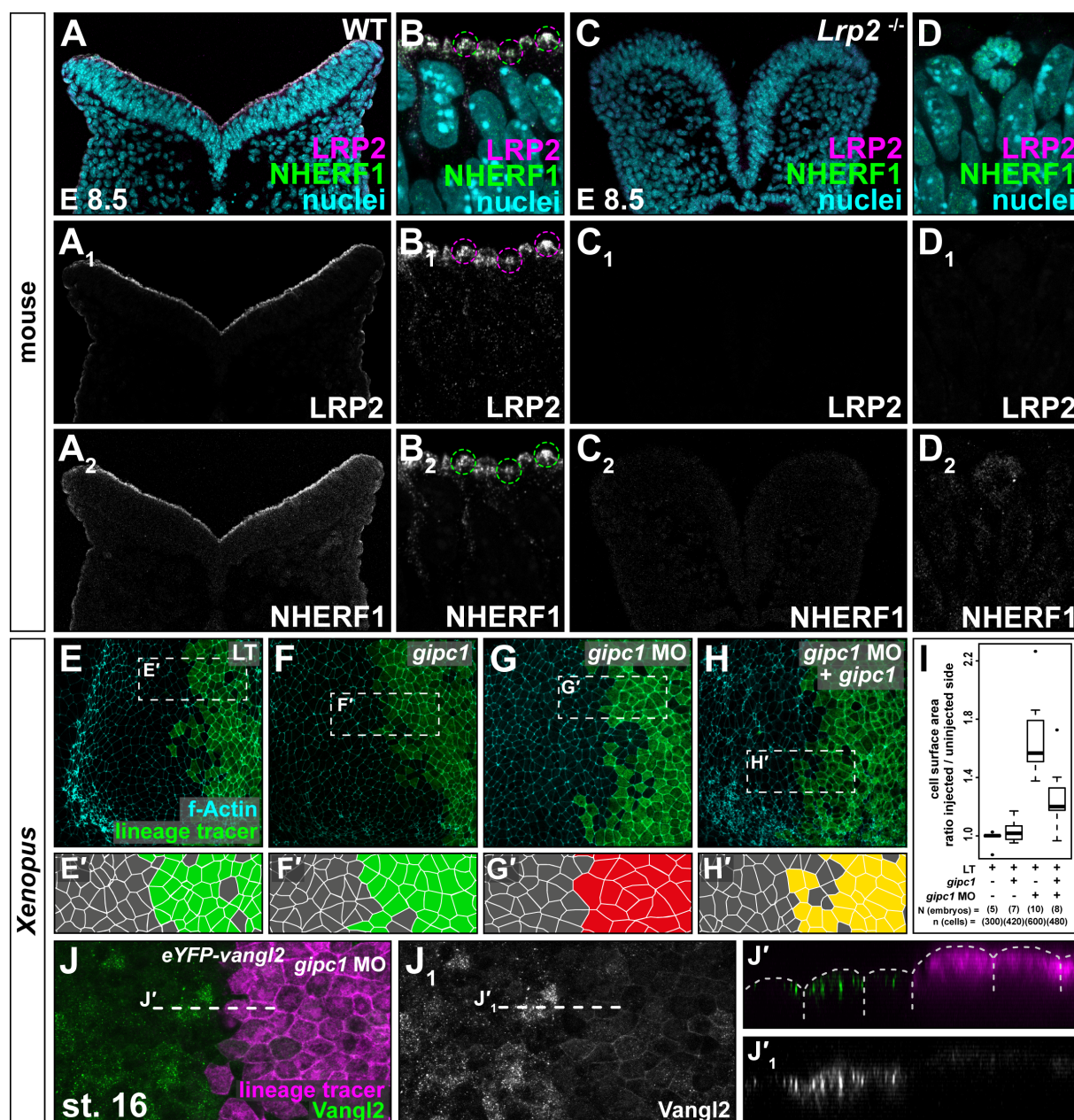
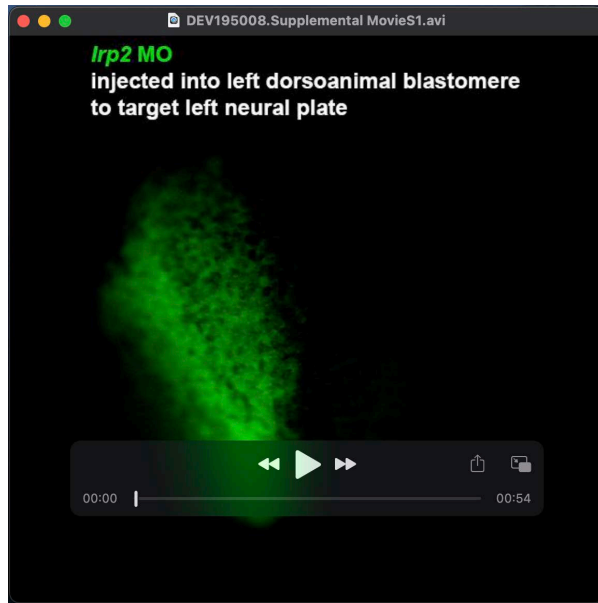
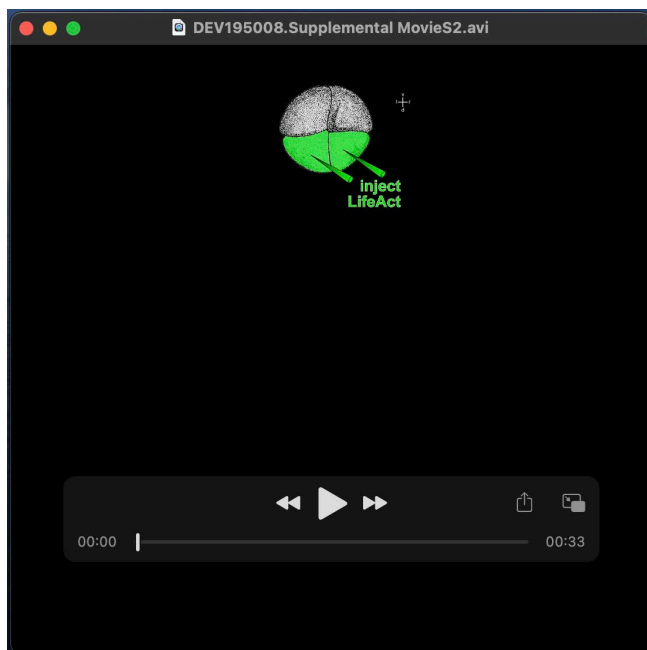


Fig. S5: Lrp2-interacting scaffold proteins in neural tube closure. (A-D) Immunofluorescence reveals co-localization of LRP2 and NHERF1 on coronal sections of wild type (WT; **A, B**) and loss of both markers in LRP2-deficient (*Lrp2*^{-/-}; **C, D**) mice at embryonic day (E) 8.5 (9 somites). (**A_{1,2} - D_{1,2}**) Channels shown in grayscale. (E-I) Morpholino oligomer (MO)-mediated *gipc1* loss-of-function (LOF) phenocopies the *Lrp2* LOF phenotype. 4-8 cell embryos were injected into one dorsal animal blastomere with lineage tracer (LT) and MO / mRNA as indicated; cell borders delineated by f-Actin staining using fluorescently labeled phalloidin. (E'-H') Cell outlines from boxes indicated in (E-H), colors represent severity of phenotype. No impairment of constriction upon injection of LT (**E, E'**) or *gipc1* (**F, F'**; green), severe impairment in MO-injected cells (**G, G'**; red), amelioration of impaired constriction upon re-introduction of *gipc1* in MO-injected cells (**H, H'**; yellow). (I) Graphical representation of experimental data from (A-D), Wilcoxon rank sum test. (J) Magnified views of forebrain area; unilateral injection of *gipc1*MO similar to (E-H). Note reduction of Vangl2 in morphant cells (10/12 embryos from 5 independent experiments), also evident in transversal optical sections (J', J'₁).



Movie 1: *Irp2* is required for neural tube closure in *Xenopus*



Movie 2: *Irp2* is required for apical constriction, but dispensable for actin dynamics in the neural plate